Applied Geochemistry 212 (2026) 107179



Contents lists available at ScienceDirect

Applied Geochemistry

journal homepage: www.elsevier.com/locate/apgeochem



Metal(loid) and dissolved organic carbon release upon redox changes during the late shoulder season in permafrost regions

Maëlle Villani [a,*], Catherine Hirst [b], Eléonore du Bois d'Aische [a], Cécile Osy [a], Maxime Thomas [a], Philippe Roux [a], Marc F. Benedetti [c], Justin Ledman [d], Edward Schuur [d], Sophie Opfergelt [a]

[a] Earth and Life Institute, Université catholique de Louvain, Louvain-la-Neuve, Belgium
[b] Department of Earth Sciences, Durham University, Durham, United Kingdom
[c] Université Paris Cité, Institut de physique du globe de Paris, CNRS, F-75005, Paris, France
[d] Center for Ecosystem Science and Society, Northern Arizona University, Flagstaff, AZ, USA

ARTICLE INFO

Editorial handling by: Jon Petter Gustafsson

Keywords:
Permafrost
Late shoulder season
Redox
metal(loid)
Dissolved organic carbon
Alaska

ABSTRACT

During the late shoulder season (i.e., the transition between summer and winter) in permafrost regions, soils shift toward more reducing conditions. This redox transition is expected to strongly influence metal(loid) and dissolved organic carbon (DOC) release to aquatic bodies, with broader implications on water quality, but also on carbon emissions. However, their release in soil waters during the late shoulder season remains poorly constrained.

We investigate how soil redox conditions influence metal(loid) and DOC release in soil pore water (capillary water; 30 cm depth) and soil water moving freely (gravitational water; 0–30 cm) at three sites spanning a natural permafrost thaw gradient dispersed between organic and mineral horizons at Eight Mile Lake (Alaska, USA). Soil waters, sampled every three days over approximately one month across the late shoulder season, were analyzed for pH, conductivity, *in situ* soil temperature and redox potential, metal(loid)s (Fe, Mn, V, As, Si; influenced by redox conditions and tracers of Fe-oxides), and δ^{30}Si and Ge/Si ratios (indirect tracers of Fe-oxides).

We show a transition from weakly to moderately reducing conditions across the late shoulder season, associated with increased metal(loid) release in soil pore waters, independent of soil properties (organic or mineral), and coupled with additional DOC release in organic soils. Where moderately reducing conditions persist in more thawed soils, metal(loid) concentrations remain high and stable in pore waters, but this signal is not reflected in freely draining water. Ongoing Arctic warming may therefore strengthen metal(loid) and DOC supply to Arctic aquatic systems.

1. Introduction

The Arctic has warmed nearly four times faster than the globe since 1979 (Rantanen et al., 2022). As a result, permafrost (i.e., frozen ground for at least two consecutive years) thaws, leading to an increase in the thickness of the active layer (i.e., the seasonally frozen surface layer; Obu, 2021; Smith et al., 2022). Permafrost soils store approximately twice as much carbon as currently present in the atmosphere, and this carbon becomes increasingly vulnerable as permafrost thaws (Schuur et al., 2022; Strauss et al., 2025). A portion of this carbon can be mobilized as dissolved organic carbon (DOC) into soil pore waters and transported through aquatic systems, exporting approximately 5% of the permafrost carbon pool annually and contributing to the permafrost carbon feedback (Plaza et al., 2019; Vonk et al., 2019) . Permafrost thaw also alters soil redox conditions, creating conditions that directly control the solubility and mobility of metal(loid)s (Drake et al., 2018; Krickov et al., 2026; Patzner et al., 2022; Walvoord and Striegl, 2007). More specifically, as permafrost thaws, the active layer deepens and ground subsidence (i.e., collapse of the land surface induced by permafrost thaw when ground ice melts) can occur, altering surface topography and leading to water saturation; the resulting soil saturation limits oxygen diffusion into the soil profile, driving conditions toward more reducing (Herndon et al., 2020). For example, under increasingly reducing conditions, Fe- and Mn-(oxyhydr)oxides, which under oxic conditions

* Corresponding author.
E-mail address: maelle.villani@uclouvain.be (M. Villani).

https://doi.org/10.1016/j.apgeochem.2026.107179
Received 25 June 2026; Received in revised form 22 September 2026; Accepted 13 November 2026
Available online 16 November 2026
0883-2927/© 2026 Elsevier Ltd. All rights are reserved, including those for text and data mining, AI training, and similar technologies.

immobilize DOC but also metal(loid)s by sorption or coprecipitation, dissolve, releasing associated metal(loid)s and DOC into solution and increasing their mobility. At larger spatial scales, the release of metal (loid)s from soils to soil pore waters can increase their transport to streams (Chupakov et al., 2023; Dial et al., 2026; Skierszkan et al., 2026), contributing to phenomena such as stream browning or rusting, often associated with increased inputs of Fe-rich, anoxic waters (Kritzberg et al., 2014; O'Donnell et al., 2024; Weyhenmeyer et al., 2014). The motivation of the study is that, the metal(loid) release into aquatic bodies, often associated with DOC release (Krickov et al., 2026) has direct consequences for aquatic ecosystems and human communities that depend on them, as well as broader implications for carbon fluxes and the permafrost carbon feedback (Miner et al., 2021; O'Donnell et al., 2024). Elevated metal(loid) concentration has been linked to measurable degradation of aquatic macroinvertebrate and fish communities in affected streams, alongside broader declines in water quality (Miner et al., 2021). Understanding the geochemistry of metal(loid) release under permafrost thaw is therefore critical not only for constraining biogeochemical cycles, but for anticipating and managing risks to Arctic water resources and food systems as warming accelerates. While much attention has been given to enhanced biogeochemical cycling of C associated with thawing permafrost, the implications of thaw on the release of metal(loid)s remain poorly resolved (Pokrovsky et al., 2016; Skierszkan et al., 2024a; Skierszkan et al., 2024b).

The impact of permafrost biogeochemical processes on metal(loid) and DOC release in soil pore waters remains poorly understood during the late shoulder season (i.e., the transitional period from the senescence of deciduous plants until the headwaters refreeze and cease to flow; Arndt et al., 2023; Shogren et al., 2020). Although Barker et al. (2014) documented late season increases in trace metal concentrations in Arctic stream waters linked to active layer deepening, the underlying redox mechanisms driving metal(loid) release in soil pore waters, and the implications for DOC, remain uncharacterized. This season is characterized by rapid environmental changes (Jentzsch et al., 2024): as soil temperatures approach near-freezing and snow begins to accumulate, oxygen diffusion decreases and soils can shift toward more reducing conditions (Bergman et al., 2025; Street et al., 2016; Villani et al., 2025). These environmental changes are expected to strongly influence the coupled release of metal(loid)s and DOC from soil to soil waters and aquatic bodies (Arndt et al., 2023).

The metal(loid)s, iron (Fe; Barker et al., 2023), manganese (Mn; Li et al., 2021), vanadium (V; Shaheen et al., 2019), arsenic (As; Catrouillet et al., 2016; Wallis et al., 2020), germanium (Ge) and silicon (Si) (Pokrovsky et al., 2014), are mobilized from soils to soil waters through changes in redox, adsorption-desorption and destabilization of organo-metal colloids. For Fe, Mn, V and As, mobility is largely controlled by redox conditions, as reducing conditions promote for example the reduction of Fe(III) to Fe(II) or As(V) to As(III), increasing their solubility (Herndon et al., 2020; Wallis et al., 2020). For Fe and Mn, the stability of interactions with organic matter can control metal (loid) and DOC release into soil pore waters (Kappler et al., 2021; Kleber et al., 2021; Mueller et al., 2015; Opfergelt et al., 2026; Yang et al., 2025). Under reducing conditions, Fe-oxides, associated with OC, can dissolve, releasing both associated metal(loid)s and DOC into soil waters, while changes in Fe speciation can further influence the stability of Fe-OC complexes (Duan et al., 2025; Liebmann et al., 2025; Patzner et al., 2020). For V (Pang et al., 2025), As (Gorny et al., 2015; Skierszkan et al., 2024b), Ge and Si (Pokrovsky et al., 2014), these metal (loid)s strongly adsorb onto Fe-oxides and can therefore be mobilized by changes in redox conditions that destabilise mineral or organo-mineral aggregates in permafrost soils. More specifically, as Fe-oxides preferentially adsorb Ge over Si, the Ge/Si ratio represents indirect proxy of Fe-oxides dissolution (Anders et al., 2003). Moreover, light silicon isotopes preferentially bind to Fe-oxides, leading to an increase in δ^{30}Si during Fe-oxides dissolution into the soil waters (Delstanche et al., 2009). It follows that Fe, Mn, V, and As serve as direct geochemical tracers of redox changes and Fe-oxides dissolution into soil pore waters, and Ge/Si ratio and δ^{30}Si serve as indirect tracers of the stability of these oxides (Lim et al., 2022; Skierszkan et al., 2024a). Together, these indicators target complementary aspects of the same process, allowing the metal(loid) release to be directly linked to Fe-oxide dissolution rather than interpreted separately.

The conditions for metal(loid) release from soil to soil water across permafrost regions are spatially heterogeneous (Herndon et al., 2020). Distinguishing between water retained in soil pores (capillary soil pore water), which reflect localized redox conditions at a specific depth, and water circulating freely (gravitational water), which integrate mixed contributions from the broader soil profile, is critical to resolve redox-driven processes during seasonal transitions (Fouché et al., 2021). At the capillary water scale, metal(loid) release into soil pore waters can supply limiting nutrients to plants and primary producers in aquatic bodies, but may also be toxic at elevated concentrations (Mauclet et al., 2022; Perryman et al., 2020). At the gravitational water scale, high metal(loid) concentrations induce harmful pollution to aquatic life once transferred to rivers (Chupakov et al., 2023; Gartler et al., 2025; O'Donnell et al., 2024). In this context, stable water isotopes (δ^{18}O and δD) represent powerful tracers of the source of gravitational waters (Mueller et al., 2014; Tan et al., 2016).

In this study, we investigate how soil redox conditions evolve during the late shoulder season and evaluate the implications for metal(loid) and DOC release into soil waters. Specifically, we monitored soil temperature and soil redox potential at 30 cm depth during the late shoulder season (September–October 2023) to follow environmental changes at three sites representing three natural stages of permafrost thaw near Eight Mile Lake, Alaska (USA). This thaw gradient allows us to evaluate how the degree of permafrost thaw, and the associated redox conditions, influence the seasonal processes of metal(loid) and DOC release during the shoulder season. We collected soil pore waters (capillary water) at 30 cm depth in both organic and mineral soil layers, and well waters (gravitational water) between 0 and 30 cm depth to be able to compare a localized pore water signal with a more integrated signal reflecting mixed hydrological pathways and redox conditions. On these samples, we measured metal(loid) concentrations (Fe, Mn, V, As, and Si) to follow metal(loid) release upon environmental changes and the mechanisms driving mobility. We further measured δ^{30}Si and Ge/Si values that are indirect tracers of Fe-oxides dissolution into the soil pore water. We also measured DOC concentrations and SUVA index (Specific UV absorbance, aromaticity index) to evaluate coupled metal(loid) and DOC release. In addition, we measured water stable isotopes (δ^{18}O and δD) in soil pore waters and well waters to trace potential contributions of capillary water to gravitational water. We hypothesize that reducing conditions during the shoulder season drive metal(loid) and DOC release into soil pore waters, depending on soil horizon properties (organic or mineral soil layer).

2. Materials and methods

2.1. Study site

The field campaign took place at the Eight Mile Lake catchment (63° 52′ N, 149° 15′ W; 700 m a.s.l., Alaska, USA) between September 15 and October 25, 2023 (Fig. 1). At the beginning of the campaign, vegetation had already entered senescence, and by its end the headwaters remained partially unfrozen. The sampling period therefore falls within, but does not span the full extent of, the late shoulder season. The site of Eight Mile Lake is characterized by a moist acidic tundra with an organic layer up to 65 cm thick (>20% OC with a mean of 40% OC; Monhonval et al., 2023) which covers cryoturbated mineral soil (<20% OC with a mean of 5% OC) that is a mixture of glacial till (small stones and cobbles) and windblown loess, and an active layer thickness between 50 and 120 cm (Kelley et al., 2021; Natali et al., 2011). The geology is composed of Tertiary sedimentary rocks, overlain by gravelly glacial till and aeolian

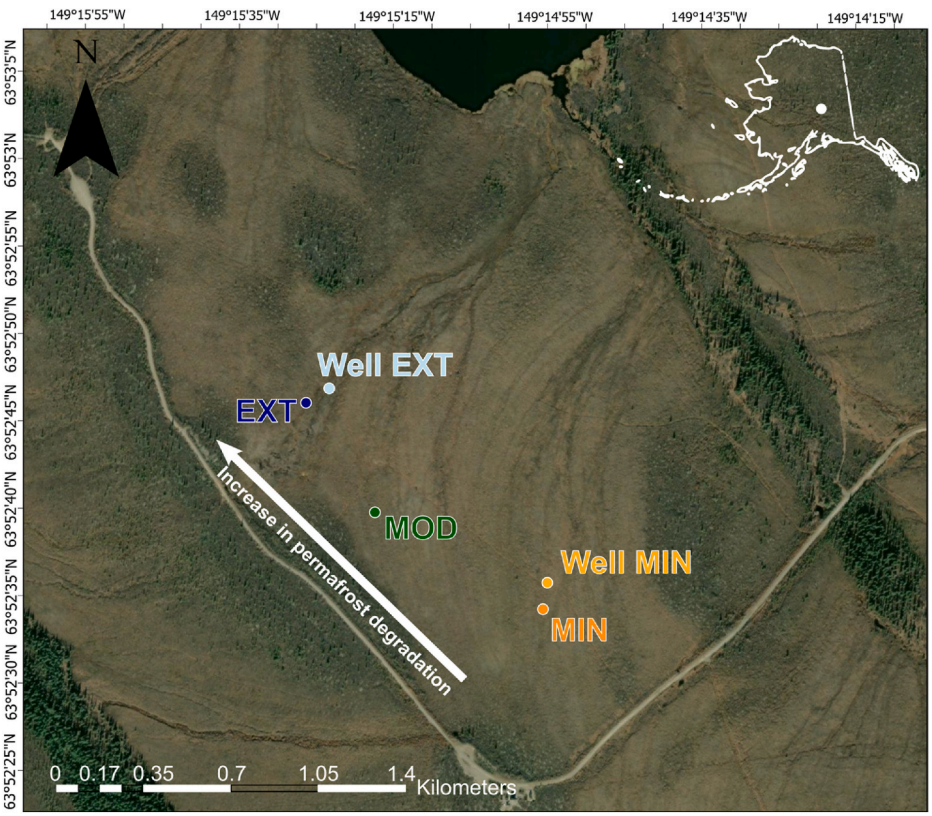


Fig. 1. Location of the study site at Eight Mile Lake (Healy, Alaska) with soil pore waters (capillary water) collection at the minimal (MIN), moderate (MOD), and extensive (EXT) sites, and well waters (gravitational water) collection at Well MIN and Well EXT sites. Soil temperature, soil water content, and redox potential were measured at the MIN, MOD, and EXT sites.

silt including the Pliocene Nenana gravel (Soil Survey Staff, 1999). The mean annual temperature in Healy is −0.9°C (1977 – 2015), with seasonal means ranging from −10.1°C (October-April) to 11.9°C (May–September; Mauritz et al., 2017). Mean annual precipitation (rain and snow) is 378 mm. Snow cover, present from mid-September to mid-May, averages 52 cm in depth (Natali et al., 2012; Osterkamp et al., 2009; Vogel et al., 2009).

The site of Eight Mile Lake is characterized as a "Gradient site", a natural gradient of permafrost thaw based on increased ground subsidence referred as the minimal (MIN), moderate (MOD) and extensive (EXT) thaw sites (Fig. 1; Monhonval et al., 2023; Osterkamp et al., 2009). More specifically, since the beginning of the monitoring (in 1990), the minimal (MIN) thaw site shows less ground subsidence (active layer depth around 50 cm depth and organo-mineral transition around 40 cm depth; Fig. S1a) and is dominated by the sedge *E. vaginatum* and *Sphagnum* sp. mosses (Mauclet et al., 2022; Schuur et al., 2007; Villani et al., 2022). The moderate (MOD) thaw site displays isolated areas of ground subsidence (active layer depth around 70 cm depth and organo-mineral transition around 20 cm depth; Fig. S1b) and remains dominated by the sedge *E. vaginatum* and mosses. The extensive (EXT) thaw site is characterized by large-scale ground subsidence (active layer depth around 90 cm depth and organo-mineral transition around 20 cm depth; Fig. S1c), with water accumulation in lower areas and drier soil conditions in higher areas, leading to shrub expansion.

2.2. Soil temperature, soil water content, and soil redox potential

The soil temperature and soil water content were monitored continuously between September 15 and October 25, 2023 at 30 cm depth in two replicates at the MIN, MOD, and EXT sites using ZL6 Pro Data Logger connected to TEROS-12 (METER group) probes with a temporal resolution of 1 h. For soil moisture measurements, the raw measurements from the sensors installed were converted to soil water content (SWC) using site-specific calibrations developed following the manufacturer's recommendations for optimal accuracy: (organic layer) $SWC\left(\frac{m^3}{m^3}\right) = 6.771 \times 10^{-10} \times RAW^3 - 5.105 \times 10^{-6} \times RAW^2 + 1.302 \times 10^{-2} \times RAW - 10.848$, and (mineral layer) $SWC\left(\frac{m^3}{m^3}\right) = 3.879 \times 10^{-4} \times RAW - 0.6956$. Soil pore water and well water samples for geochemical analyses were collected every three days and sensor data were averaged over the corresponding sampling intervals so that each water sample was associated with a single representative value of soil temperature and soil water content. This temporal aggregation ensured consistency between environmental variables and water chemistry data, allowing direct comparison among sites and subsequent multivariate analyses (e.g., PCA and correlation matrix).

The soil redox potential was monitored at the 30 cm depth at the MIN, MOD, and EXT site using a redox probe ORP-40-4-D (SWAP instruments; integrated reference electrode: Ag/AgCl, 3 M KCl at 25°C) every 30 min. Data was processed to report data as Eh *versus* the standard hydrogen electrode (SHE): A correction of +208 mV was applied to all raw values in the data set as recommended by the electrode manufacturer. Redox potential was not corrected for temperature; the sites were consistently cold, thus these corrections would have minimal influence on interpretation (following the same method as Sutor et al., 2025). Data were also averaged over the corresponding sampling intervals so that each water sample was associated with a single representative value of soil redox potential.

2.3. Water sampling

Capillary water samples from soil pore waters (n = 27) were

collected at the same locations as the soil temperature and soil redox potential measurements, the MIN, MOD, and EXT sites, at 30 cm depth between September 15 and October 25, 2023. To collect the soil pore water, we used macrorhizons with a pore size of 0.15 μm and a 10 cm porous part inserted to the specified depth (Rhizosphere, Wageningen, The Netherlands) connected to a 60 mL polypropylene syringe (BD Plastipak luer lock). One soil pore water sample corresponds to a bulk of three to four consecutive days of water collection. Due to drier conditions at the MIN site (n = 7), fewer samples were collected compared to the MOD (n = 9), and EXT (n = 11) sites. Because syringe filling required up to 24 h and no in-field acidification of the accumulating sample was possible, dissolved Fe(II) was subject to progressive oxidation prior to recovery; Fe(II)/Fe(III) speciation was therefore not considered a reliable redox indicator for this sampling design.

Gravitational waters were collected from wells (n = 26) at the Well MIN and Well EXT sites every three days during the sampling period. The wells were drained of standing water, left to refill with laterally flowing active layer waters and subsequently sampled into preconditioned 10 L containers using a battery-operated pump. Well water was filtered at 0.7 μm with glass fiber filters to measure the DOC concentration, and at 0.22 μm (or 0.8 μm for Fe nanoparticles) with cellulose acetate filters to measure all the other chemical elements, while water isotopes were measured on unfiltered samples. Pore size tests were conducted for DOC (0.45 μm with glass fiber filters) and Fe (0.40 μm with cellulose acetate filters) to assess the potential effect of filter pore size on measured concentrations (Villani et al., 2026). These results indicated that the difference in pore size used for DOC measurements in well water (0.70 μm) and soil pore water (0.15 μm; Villani et al., 2026) is unlikely to introduce a substantial bias in the reported DOC concentrations. As with pore-water sampling, the pumping and filtration steps introduced brief atmospheric exposure sufficient to shift the Fe(II)/Fe(III) equilibrium, precluding a reliable direct redox speciation measurement on these samples.

2.4. Chemical analyses

2.4.1. pH and electrical conductivity measurements

In soil pore waters (n = 27), pH and electrical conductivity ("conductivity" in the text) were measured in the laboratory (UCLouvain, Belgium) within one month using a SevenCompact™ Duo S213 probe in a clean room. In well waters (n = 26), the pH and electrical conductivity were directly measured on the field using a probe from HANNA Instruments (HI991300).

2.4.2. Major and trace element concentrations

Concentrations in Fe, Mn, and Si were measured in soil pore waters (n = 27) and wells waters (n = 26) acidified with 2% HNO_3 suprapur using an inductively coupled plasma-optical emission spectrometer (ICP-OES, iCAP 6500 ThermoFisher Scientific). The accuracies were ± 2% for Fe, ± 3% for Mn, and ± 1% for Si and were assessed using the water reference material SLRS-4 (Yeghicheyan et al., 2001). The detection limit is 0.001 mg L^{-1} for Fe, 0.001 mg L^{-1} for Mn, and 0.002 mg L^{-1} for Si.

Concentrations in V, As, and Ge were measured in soil pore waters (n = 27) and well waters (n = 26) acidified with 2% HNO_3 suprapur using ICP-MS (iCAP Q ICP-MS, Thermo Fisher Scientific, Waltham, MA, USA). The accuracy on element concentrations (±1% for V, ±15% for As, and ±8% for Ge) was assessed using the water reference material SLRS-4 (Yeghicheyan et al., 2001). The detection limits were estimated to 0.003 μg L^{-1} for V, 0.01 μg L^{-1} for As, and 0.001 μg L^{-1} for Ge. The precision of the Ge/Si ratio is ±8%.

2.4.3. Iron nanoparticles analysis

Iron nanoparticles (NPs), defined as particles < 100 nm (Wigginton et al., 2007), were analyzed as part of the colloidal fraction (1–1000 nm; PAC, 1972) in well water samples collected at the Well MIN (n = 1) and Well EXT sites (n = 4). Samples were filtered within 24h of sampling at 0.8 μm on cellulose acetate filters, preserved in the fridge at 4°C, and diluted 10000-fold in Milli-Q water prior to analysis. Results on Fe nanoparticles at the Well MIN site rely on a single sample from the beginning of the sampling period, while the four samples at the Well EXT site were collected at the beginning and at the end of the sampling period, allowing temporal analysis.

Iron-bearing colloids in 0.8 μm–filtered solutions were quantified by single-particle high-resolution ICP-MS (spHR-ICP-MS; Element II, Thermo Scientific) at the IPGP PARI platform. Instrumental settings are provided in Table S1. Samples were diluted 10000-fold and analyzed for 6 min to limit coincident particle detection. Between measurements, the introduction system was rinsed with 1% HNO_3 (v/v) for 2 min and ultrapure water for 5 min.

Transport and nebulization efficiencies were determined using 60 nm Au nanoparticle standards (BBI Solutions, UK; 2.6×10^5 particles mL^{-1}) and dissolved Au standards (0–20 ng mL^{-1}). Transport efficiency ($\eta_{transport}$) represents ion losses between the plasma and detector, whereas nebulization efficiency ($\eta_{nebulization}$) accounts for particle losses during aerosol formation (Tharaud et al., 2021). Transport and nebulization efficiencies ranged from 3.7 to 4.8% and from 3.7 to 4.4%, respectively.

External calibration for Al and Fe (0–20 μg L^{-1}, in 2% HNO_3) was performed at the beginning of each analytical sequence to convert pulse intensity into elemental mass (Cornelis and Hassellöv, 2014; Moreira-Álvarez et al., 2023; Tharaud et al., 2017). To separate particle-associated pulses from the dissolved/ionic background, the time-resolved intensity distribution of each sample was deconvoluted using a Gaussian mixture model based on a mixed poly-Gaussian probability mass function, following Tharaud et al. (2021). The model was fitted to the low-intensity region of the time-resolved dataset, representing the ionic background, and the fitted background distribution was subtracted from the total distribution to retrieve the particle-signal distribution. The number of fitted values corresponded to all dwell-time signals assigned to the low-intensity background component in each sample; it was therefore sample-specific and not fixed a priori. Dissolved Al and Fe calibration standards were used for mass calibration, whereas the deconvolution was conducted independently on each unknown sample. Pulse intensity was converted to elemental mass per particle and pulse frequency to particle number concentration.

Particle-event intensity was converted to elemental mass using the dissolved Al or Fe calibration curve after subtraction of the fitted ionic-background contribution. Elemental masses were converted to equivalent spherical diameters according to: $d_{eq} = \left(\frac{6m_{el}}{\pi \rho f_{el}}\right)^{\frac{1}{3}}$; where m_{el} is the elemental mass per event, ρ is the density of the assumed particle phase, and f_{el} is the corresponding elemental mass fraction. Fe sizes were calculated using: Fe_2O_3, Fe fraction = 0.699, density = 5.24. Values are therefore reported as equivalent spherical diameters and should not be interpreted as direct physical-size measurements of compositionally heterogeneous environmental colloids.

The lower particle-mass cutoff was derived from the fitted dissolved/ionic-background distribution for each sample. Signals below this sample-specific decision threshold were retained in the total signal distribution but were not assigned as individual particle events, because they could not be reliably distinguished from ionic background. The cutoff was converted to elemental mass using the relevant dissolved-element calibration and is displayed in Fig. S7 as the method-specific particle-mass detection limit.

2.4.4. Silicon isotope analysis

The silicon isotope composition ($\delta^{30}Si$) was measured in soil pore waters (n = 27) and well waters (n = 26) using a MC-ICP-MS (Neptune Plus™ High Resolution Multicollector ICP-MS, Thermo Fisher Scientific, Earth & Life Institute, UCLouvain, Belgium) following the same method

as Hirst et al. (2023). Sample preparation was done in clean lab conditions (ISO 6) under a laminar flow hood (ISO 5). A volume equivalent to 10 µg Si was dried down. The dissolved organic carbon in solution was removed by repeated cycles of heating (60°C) with concentrated HNO_3 and H_2O_2 and evaporating (80°C) cycles (Hughes et al., 2011). The sample was digested in 0.125 M NaOH for 4 h at 100°C, then acidified with HNO_3. Silicon was purified from the matrix with a one-stage column chemistry using a cation exchange resin (Biorad AG50W-X12; Georg et al., 2006). The Si recovery was typically > 90% and Na^+ concentrations below the detection limit.

The silicon isotope composition ($\delta^{30}Si$) was measured by MC-ICP-MS in wet plasma mode in high resolution ($\Delta m/m \approx 9000$) using a PFA nebulizer of 100 µL min^{-1} uptake rate. The instrumental mass bias was corrected using the standard-sample bracketing technique and an external Mg doping (Cardinal et al., 2003). The analyses were performed in 2% HNO_3 matrix, with a typical sensitivity of 3.5 V for 1 mg L^{-1} Si and an instrumental blank < 30 mV. The $\delta^{30}Si$ compositions are expressed in relative deviations of $^{30}Si/^{28}Si$ ratio from an in-house standard (Quartz Merck) isotopically similar to NBS28 reference standard using the common δ-notation (‰) as follows (Abraham et al., 2008):

$$\delta^{30}Si = \left[\frac{\left(^{30}Si/^{28}Si\right)_{sample}}{\left(^{30}Si/^{28}Si\right)_{NBS28}} - 1\right] \times 1000$$

The long-term precision and accuracy of the MC-ICP-MS was assessed from diatomite standard measurements ($\delta^{30}Si = 1.27 \pm 0.07$‰; SD; n = 69) which are consistent with previously reported values ($\delta^{30}Si = 1.26 \pm 0.10$‰; Reynolds et al., 2007).

2.4.5. Water isotopes measurements

In well waters (n = 26), oxygen ($\delta^{18}O$) and deuterium (δD) isotopes values (Fig. S3) were determined on unfiltered samples using Cavity Ring Down Spectroscopy on a Liquid Water Isotope Analyzer (L2130-i, Picarro®). Values are normalized between SLAP and VSMOW and reported in per mil deviation relative to VSMOW. The reproducibility is ± 0.1‰ for $\delta^{18}O$ and ± 0.6‰ for δD.

2.4.6. Dissolved organic carbon concentration and SUVA index measurements

The concentration in dissolved organic carbon (DOC) in soil pore waters (n = 27) and well waters (n = 26) was measured using high-temperature catalytic oxidation (Shimadzu® TOC-VCPH) with a detection limit of 0.1 mg L^{-1} and accuracy of ± 2%. Samples were stored at 4°C prior to analysis. Upon return from the field, samples were acidified to 2% HNO_3 and sonicated in an ultrasonic bath to ensure homogenization, and were analyzed within one month.

The SUVA index (specific ultraviolet absorbance; in L mg^{-1} m^{-1}), a proxy of carbon aromaticity, was measured in soil pore waters (n = 27) and well waters (n = 26). This index was calculated as follows: SUVA = A_{254}/(b x DOC), where A_{254} is the sample absorbance at 254 nm (non-dimensional), b is the optical path length (m) and DOC concentration (mg L^{-1}). The absorbance was measured on a Thermo Scientific Genesys 10S UV-Vis Spectrophotometer with a wavelength accuracy of ± 0.2 nm and a wavelength repeatability of ± 0.05 nm. SUVA values were corrected for Fe interference in samples when Fe concentrations exceeded 2 mg L^{-1} (Poulin et al., 2014; Wauthy et al., 2018). The precision of the SUVA values is ±2%.

2.5. Data treatment

All graphs and statistics were performed using R 4.0.2 (RStudio Inc., Boston, Massachusetts, USA) and plots using the ggplot2 package.

The significant trend in soil temperature, soil redox potential, pH, conductivity, concentrations in Fe, Mn, V, As and Si, $\delta^{30}Si$ and Ge/Si values, DOC concentrations, SUVA index, and $\delta^{18}O$ values along the late shoulder season were evaluated using a non-parametric Mann-Kendall test. The significant differences in variables between the MIN, MOD, and EXT sites were evaluated using a non-parametric Kruskal–Wallis tests followed by Dunn's post-hoc tests with Bonferroni correction. The significant differences in variables between the Well MIN and Well EXT sites were evaluated using a non-parametric Wilcoxon test. The 95% confidence intervals of the statistic were used to test for a significant difference or trend between values, which is equivalent to a p-value cutoff of 0.05 (* if p-value < 0.05; ** if p-value < 0.01; *** if p-value < 0.001).

A Principal Component Analysis (PCA) was conducted using soil temperature, soil redox potential, pH, conductivity, Fe, Mn, V, As and Si concentrations, $\delta^{30}Si$ and Ge/Si values, DOC concentrations, and SUVA index in soil waters using R 4.0.2. Spearman rank correlation matrices were computed separately for each site using R 4.0.2. For each variable pair, the correlation coefficient (r) and corresponding p-value were calculated (* if p-value < 0.05; ** if p-value < 0.01; *** if p-value < 0.001).

3. Results

3.1. Soil temperature and soil redox potential

Along the late shoulder season, soil temperature varies from 1.9 to 0.1°C (0.4 ± 0.5°C; Fig. 2a). Soil temperature significantly decreases along the season (Mann-Kendall test) at the MIN (p-value < 0.001), MOD (p-value < 0.05), and EXT sites (p-value < 0.01). Moreover, the near-freezing period appears around October 1, where soil temperature reaches 0.1°C. Soil temperature is significantly higher (mean differences of only ~ 0.2°C) at the MIN site than at the EXT site (Kruskal-Wallis and Dunn tests; p-value < 0.01).

Soil redox potential varies from 311 to −94 mV (51 ± 107 mV; Fig. 2b). Soil redox potential significantly decreases along the season (Mann-Kendall test) at the MIN (p-value < 0.01), MOD (p-value < 0.001), and EXT sites (p-value < 0.001). Moreover, soil redox potential is significantly higher at the MIN site than the EXT site (Kruskal-Wallis and Dunn tests; p-value < 0.001).

3.2. pH and conductivity in the soil waters

The pH values vary between 2.9 and 6.4 (5.3 ± 1.6) in soil pore waters, and between 4.4 and 5.3 (4.8 ± 0.2) in well waters along the late shoulder season (Fig. 3a). The pH values in soil pore waters and well waters remain similar along the late shoulder season for all sites (Mann-Kendall test; p-value > 0.05). More specifically in soil pore waters, pH values at the MIN site are significantly lower (Kruskal-Wallis and Dunn tests) than pH values at the MOD (p-value < 0.001) and EXT sites (p-value < 0.01). The lower pH values observed at the MIN site at 30 cm

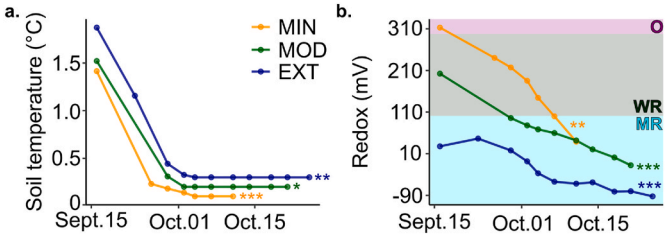


Fig. 2. Soil temperature (in °C; **a.**) and soil redox potential (in mV; O for oxidized, WR for weakly reduced, and MR for moderately reduced conditions; following the classification of Liebmann et al., 2025; **b.**) measured at 30 cm depth at the MIN, MOD, and EXT sites between September 15 and October 25, 2023. Mann-Kendall test was performed to identify significant temporal trends for each site (* if p-value < 0.05, ** if p-value < 0.01, and *** if p-value < 0.001). Kruskal-Wallis and Dunn tests were performed to identify significant differences between the MIN, MOD and EXT sites and the results are reported in Table S3.

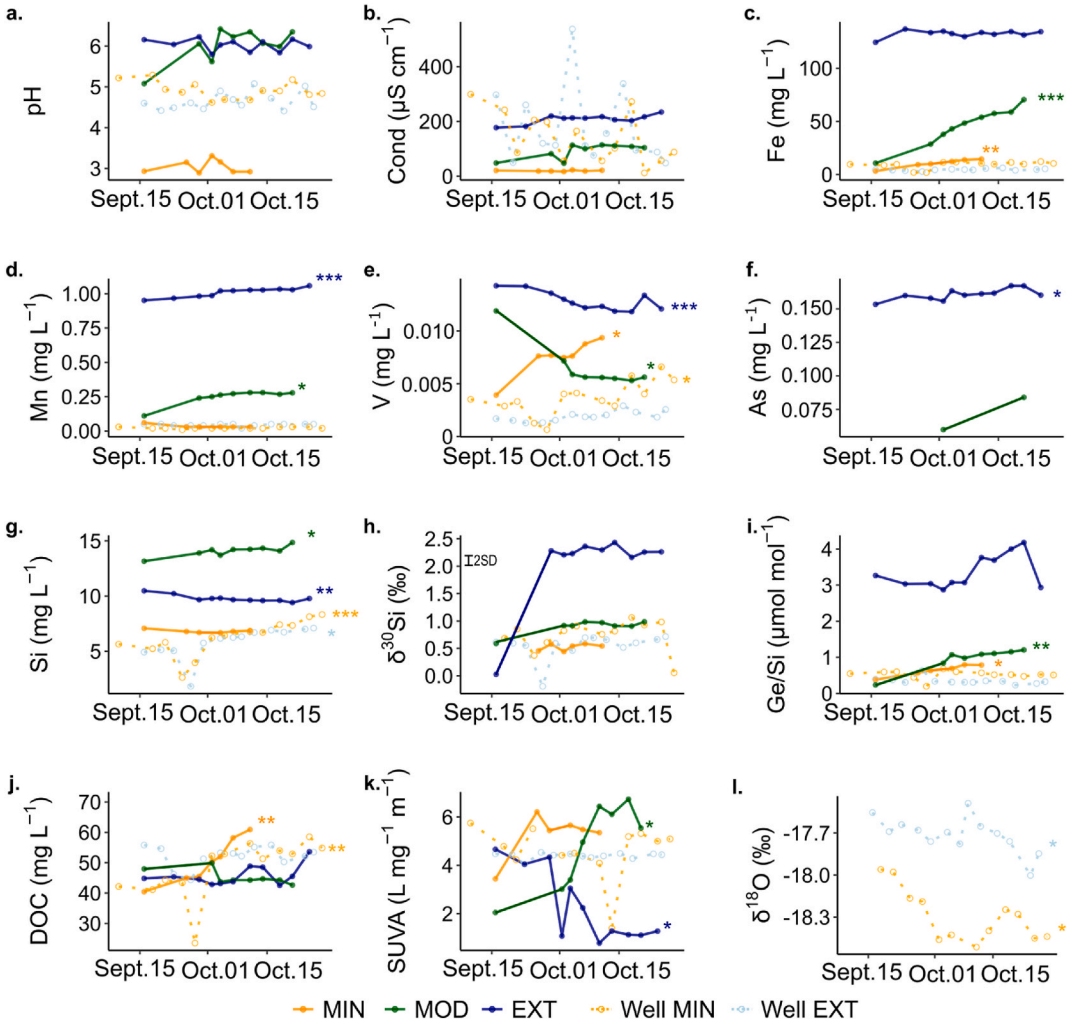


Fig. 3. Values of pH (**a.**) and electrical conductivity (in µS cm^{-1}; **b.**), concentrations in Fe (in mg L^{-1}; **c.**), Mn (in mg L^{-1}; **d.**), V (in mg L^{-1}; **e.**), As (in mg L^{-1}; most of the results were <DL; **f.**), and Si (in mg L^{-1}; **g.**), values of $\delta^{30}Si$ (in ‰; **h.**) Ge/Si (in µmol mol^{-1}; the error bar corresponds to the standard deviation (2SD); **i.**), concentrations in DOC (in mg L^{-1}; **j.**) and SUVA values (in L mg^{-1} m^{-1}; **k.**), and values of $\delta^{18}O$ (in ‰; **l.**) measured in soil pore waters (capillary waters) at 30 cm depth at the MIN, MOD, and EXT sites (solid lines), and in well waters (gravitational waters) at the Well MIN and Well EXT sites (0-30 cm depth; dashed lines) between September 15 and October 25, 2023. Analytical error is smaller than symbol size except for As concentrations (±15%) and Ge/Si values (±8%). Mann-Kendall test was performed to identify significant temporal trends for each site (* if p-value < 0.05, ** if p-value < 0.01, and *** if p-value < 0.001). Kruskal-Wallis and Dunn tests were performed to identify significant differences between the MIN, MOD and EXT sites and the results are reported in Table S3. Wilcoxon test was performed to identify significant differences between the Well MIN and the Well EXT sites and the results are reported in Table S4.

depth, together with darker soil coloration (Fig. S1a), supports the presence of an organic horizon at that depth. In contrast, at the MOD and EXT sites, the 30 cm depth is located within the mineral horizon, as supported by pH values and soil profile observations (Fig. S1b–c). These horizon differences are also directly reflected in the soil water content (Fig. S2), with the MIN site (around 0.94 m^3 m^{-3}) exhibiting a significantly higher soil water content than the MOD (around 0.45 m^3 m^{-3}) and EXT (around 0.48 m^3 m^{-3}) sites.

Electrical conductivity in soil pore waters varies between 17 and 234 µS cm^{-1} (121 ± 81.3 µS cm^{-1}) and between 12 and 537 µS cm^{-1} (171 ± 118 µS cm^{-1}) in the well waters (Fig. 3b). Conductivity in soil pore waters and well waters remain similar along the late shoulder season for all sites (Mann-Kendall test; p-value > 0.05). More specifically, in soil pore waters, conductivity at the MIN site is significantly lower (Kruskal-Wallis and Dunn tests) than soil pore water conductivity at the EXT site (p-value < 0.001).

3.3. Direct tracers of redox changes: metal(loid) concentrations in soil waters

In soil pore waters, Fe concentrations vary between 3.27 and 137 mg L^{-1} (74.2 ± 53.6 mg L^{-1}; Fig. 3c), Mn concentrations vary between 0.03 and 1.06 mg L^{-1} (0.52 ± 0.43 mg L^{-1}; Fig. 3d), V concentrations vary between 0.003 and 0.014 mg L^{-1} (0.009 ± 0.003 mg L^{-1}; Fig. 3e), As concentrations vary between 0.059 and 0.167 mg L^{-1} (0.147 ± 0.034 mg L^{-1}; Fig. 3f), and Si concentration varies between 6.68 and 14.8 mg L^{-1} (10.6 ± 2.86 mg L^{-1}; Fig. 3g) along the late shoulder season. The concentrations in Fe, Mn, V, and As at the EXT site are significantly higher (Kruskal-Wallis and Dunn tests) than at the MIN and the MOD sites (p-value < 0.05). The Si concentration in soil pore waters at the MOD site is significantly higher (Kruskal-Wallis and Dunn tests) than at the MIN (p-value < 0.001) and EXT sites (p-value < 0.05). Moreover, Fe concentrations in soil pore waters significantly increase (Mann-Kendall test) at the MIN (p-value < 0.01) and the MOD sites (p-value < 0.001) along the late shoulder season. The Mn concentrations in soil pore waters significantly increase (Mann-Kendall test) at the MOD (p-value < 0.05) and the EXT sites (p-value < 0.001) along the late

shoulder season. The V concentrations in soil pore waters significantly increase (Mann-Kendall test) at the MIN site (p-value < 0.05), and significantly decreases at the MOD (p-value < 0.05) and EXT sites (p-value < 0.001) along the late shoulder season. The Si concentration significantly increases (Mann-Kendall test) at the MOD site (p-value < 0.05) and significantly decreases at the EXT site (p-value < 0.01) along the late shoulder season. These results reflect higher metal(loid) concentrations at the EXT site than at the MIN and MOD sites and an increase in metal(loid) concentrations along the late shoulder season mainly at the MIN and MOD sites.

In well waters, Fe concentrations vary between 1.52 and 12.2 mg L^{-1} (6.52 ± 3.37 mg L^{-1}; Fig. 3c), Mn concentrations vary between 0.01 and 0.07 mg L^{-1} (0.03 ± 0.02 mg L^{-1}; Fig. 3d), V concentration varies between 0.0007 and 0.01 mg L^{-1} (0.003 ± 0.002 mg L^{-1}; Fig. 3e), As concentrations are below the detection limit (Fig. 3f), and Si concentration varies between 1.82 and 8.33 mg L^{-1} (5.99 ± 1.48 mg L^{-1}; Fig. 3g). In well waters, metal(loid) concentrations are significantly different between the Well EXT site and the Well MIN site (Wilcoxon test, p-value < 0.05). However, concentrations at the Well EXT are not higher than at the Well MIN, in contrast to concentrations in soil pore waters. Moreover, only V concentrations at the Well MIN site significantly increase along the late shoulder season (Mann-Kendall test, p-value < 0.05).

In well waters, the Fe nanoparticle mass ranges from 0.05 to 0.1 fg (Fig. S7), corresponding to an estimated size ranging between 23 and 29 nm (Table S2). The Fe nanoparticles mass is significantly higher at Well MIN (0.1 ± 0.26 fg) than at Well EXT (0.07 ± 0.31 fg; Wilcoxon test; p-value < 0.01).

3.4. Indirect tracers of redox changes: Ge/Si and silicon isotope values in soil waters

The $\delta^{30}Si$ values vary between 0.03 and 2.43‰ (1.28 ± 0.82‰) in soil pore waters and between −0.19 and 1.06‰ (0.64 ± 0.27‰) in well waters (Fig. 3h). The $\delta^{30}Si$ values in soil pore waters and well waters are not significantly different along the late shoulder season for all the sites (Mann-Kendall test; p-value > 0.05). However, the $\delta^{30}Si$ values in soil pore waters at the EXT site are significantly higher than $\delta^{30}Si$ values at the MIN site (Kruskal-Wallis and Dunn tests, p-value < 0.001) across the shoulder season.

The Ge/Si ratio varies between 0.23 and 4.18 μmol mol^{-1} (1.93 ± 1.33 μmol mol^{-1}) in soil pore waters and between 0.19 and 0.68 μmol mol^{-1} (0.42 ± 0.13 μmol mol^{-1}; Fig. 3i) in well waters. In soil pore waters, the Ge/Si ratio at the EXT site is significantly higher (Kruskal-Wallis and Dunn tests) than at the MIN (p-value < 0.001) and MOD sites (p-value < 0.01). In soil pore waters, the Ge/Si ratio significantly increases along the late shoulder season (Mann-Kendall test) at the MIN (p-value < 0.05) and MOD sites (p-value < 0.01). In contrast, in well waters, the Ge/Si ratios are not significantly different along the late shoulder season or between the different sites.

3.5. Concentrations in DOC and SUVA index in soil waters

Along the late shoulder season, DOC concentrations vary between 40.4 and 60.9 mg L^{-1} (46.8 ± 4.9 mg L^{-1}) in soil pore waters and between 23.5 and 70.9 mg L^{-1} (50.2 ± 8.6 mg L^{-1}) in well waters (Fig. 3j). The DOC concentrations significantly increase at the MIN site in soil pore waters and at the Well MIN in well waters along the late shoulder season (Mann-Kendall test; p-value < 0.01). Moreover, in soil pore waters and well waters, DOC concentrations are not significantly different between all the sites (Kruskal-Wallis and Dunn tests; p-value > 0.05).

The SUVA index varies between 0.78 and 6.73 L mg^{-1} m^{-1} (3.79 ± 1.98 L mg^{-1} m^{-1}) in soil pore waters and between 1.40 and 5.75 L mg^{-1} m^{-1} (4.50 ± 0.78 L mg^{-1} m^{-1}) in well waters (Fig. 3k). In soil pore waters, SUVA index significantly increases at the MOD site and significantly decreases at the EXT site (Mann-Kendall test; p-value < 0.05) along the late shoulder season. Moreover, in soil pore waters, SUVA index at the EXT site is significantly different (Kruskal-Wallis and Dunn tests) than at the MOD site (p-value < 0.05). In well waters, SUVA index at the Well EXT site is significantly lower (Wilcoxon test) than at the Well MIN site (p-value < 0.05).

3.6. Water isotopes in well waters

In well waters, $\delta^{18}O$ values vary between −18.51 and −17.49‰ (−17.99 ± 0.33‰; Fig. 3l). The $\delta^{18}O$ values significantly decrease along the late shoulder season for both the Well MIN and Well EXT sites (Mann-Kendall test; p-value < 0.05). Moreover, $\delta^{18}O$ values at the Well EXT site are significantly higher than $\delta^{18}O$ values at the Well MIN site (Wilcoxon test, p-value < 0.05).

3.7. Principal component analysis of soil temperature, soil redox potential and soil water variables

The PCA shows patterns in soil physical and soil pore water geochemical properties for the 27 soil pore water samples (Fig. 4a) where PC 1 explains 52.9% of all data set variation. This PC1 is dominated by redox-sensitive metal(loid)s (Fe, Mn, V, and As concentrations) and $\delta^{30}Si$ and Ge/Si values which can vary depending on redox-driven oxide dissolution. All soil pore waters from the EXT site are in the right hand side of the PCA, corresponding to low redox potential and high concentrations of Fe, Mn, V, and As, and high $\delta^{30}Si$ and Ge/Si values. All soil pore waters from the MIN site are in the left hand side of the PCA, corresponding to the opposite redox conditions than the EXT site, and soil pore waters from the MOD site lie closer to the MIN site than to the EXT site. The PC2 from soil pore waters explains 19.8% of all data set variation and is dominated by Si concentrations. The PC3 from soil pore waters explains 11% of all data set variation (Fig. S4a) and is dominated by soil temperatures, negatively correlated to DOC concentration. Because soil temperature responds to decreasing air temperature occurring during the late shoulder season, this component evidences a clear influence of seasonal change on soil pore water chemistry. Soil pore waters collected in the beginning of the late shoulder season, in the upper quadrant, are associated with higher soil temperatures and lower DOC concentrations. Soil pore waters collected later during the late shoulder season, in the lower quadrant, are associated with low soil temperatures and high DOC concentrations.

In contrast, the well water PCA does not show the same structure as the soil pore water PCA (Fig. 4b and Fig. S4b). Importantly, redox-sensitive metal(loid)s such as Fe, Mn, V, and As point in diverging directions, indicating that redox potential is not the dominant control on well water metal(loid) concentrations.

3.8. Relationships between DOC, metal(loid) concentrations, soil temperature and soil redox potential

At the MIN site, DOC concentrations in soil pore waters are strongly coupled to redox changes (Fig. S5a). More specifically, DOC concentrations are significantly positively correlated with Fe (Spearman; $r = 1$; p-value < 0.001), V ($r = 0.77$; p-value < 0.05), and Ge/Si values ($r = 0.94$; p-value < 0.01) and negatively correlated with soil temperature ($r = -0.96$; p-value < 0.001) and redox potential ($r = -1$; p-value < 0.001). In well waters, DOC concentrations are significantly negatively correlated with soil temperature ($r = -0.76$; p-value < 0.01), redox potential ($r = -0.82$; p-value < 0.01), pH ($r = -0.64$; p-value < 0.05), conductivity ($r = -0.56$; p-value < 0.05) and $\delta^{18}O$ ($r = -0.76$; p-value < 0.01), and positively correlated with Fe ($r = 0.82$; p-value < 0.001), V ($r = 0.8$; p-value < 0.001), and Si concentrations ($r = 0.91$; p-value < 0.001; Fig. S6a).

At the MOD site, DOC concentrations in soil pore waters are not correlated with redox-sensitive elements but exhibit a significant

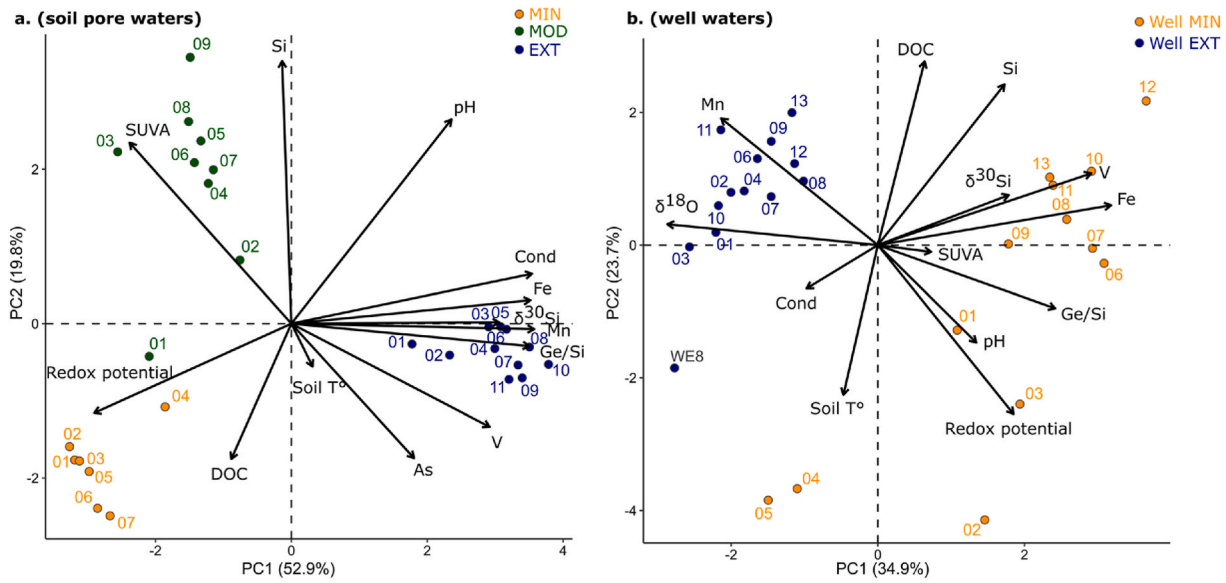


Fig. 4. PCA ordination diagram of soil physical and soil pore water (a.) and well water (b.) chemical response variables (solid black arrows) and soil pore waters (yellow, green and blue symbols; capillary waters) or well waters (yellow and blue; gravitational water). PCs 1 and 2 explain 52.9 and 19.8% of total data set variance in soil pore waters, respectively. PCs 1 and 2 explain 34.9 and 23.7% of total data set variance in well waters, respectively. Vector lengths were adjusted for visualization and may exceed unity. See Table S5 and Table S6 for nominal soil pore waters and well waters description.

negative correlation with pH ($r = -0.87$; p-value < 0.05) and a positive correlation with soil temperature ($r = 0.73$; p-value < 0.05; Fig. S5b).

At the EXT site, DOC concentrations in soil pore waters show no significant correlations with all the measured parameters (Spearman, p-value > 0.05; Fig. S5c). In well waters, DOC concentrations exhibit a significant positive correlation with Fe concentration ($r = 0.75$; p-value < 0.001; Fig. S6b).

4. Discussion

4.1. Changes in soil redox conditions along the late shoulder season influenced by permafrost thaw

Soil temperatures evolve similarly at the three sites (MIN, MOD, and EXT sites) during the late shoulder season despite contrasted stages of permafrost thaw (Fig. 2a). This similarity likely reflects the high soil moisture content at all three sites (Fig. S2), which, despite contrasting horizon properties between sites, remains high to buffer the soil thermal regime through the high heat capacity of water and latent heat effects associated, thereby limiting temperature divergence (O'Donnell et al., 2009). However, differences in permafrost thaw, soil horizon characteristics, and water saturation can create distinct redox environments, with the more extensively thawed EXT site experiencing more persistent reducing conditions than the MIN and MOD sites. Such spatial heterogeneity is therefore important to consider when assessing the effects of redox changes on metal(loid) and DOC release.

Redox conditions in this study were assessed through different indicators, each capturing a different facet of the same underlying biogeochemical process. Redox potential, measured directly *in situ* with a probe, provides a real-time, continuous physico-chemical measurement of the prevailing redox state, but it is a point measurement sensitive to local microsite heterogeneity and to short-term fluctuations (e.g., following precipitation events), and does not by itself indicate which redox-sensitive phases are reacting (Fernandez et al., 2019). At our sites, redox potential declines progressively over the late shoulder season at the minimal (MIN) and moderate (MOD) thawed sites, from weakly to moderately reduced conditions, whereas at the extensive (EXT) thaw site it remains persistently within the moderately reduced range throughout the season (Fig. 2b), pointing to an actively evolving redox regime at the MIN and MOD sites *versus* an already-reduced, stable regime at the EXT site (Liebmann et al., 2025; Patzner et al., 2022; Reddy et al., 2022). This highlights that the EXT site has greater ground subsidence, and a longer duration of soil saturation during the preceding growing season (Schuur et al., 2007). Consequently, the EXT site could potentially release metal(loid)s into soil waters throughout the year (until the active layer totally freezes) whereas the metal(loid) release into soil waters at the MIN and MOD sites is driven by seasonal redox shifts (Barczok et al., 2024; Liebmann et al., 2025).

Concentrations of redox-sensitive metal(loid)s (Fe, Mn, As and V; Fig. 3c–f) in soil pore waters serve as direct chemical indicators of ongoing reduction as rising concentrations of these elements in solution directly reflect the occurrence and progression of reductive dissolution. Consistent with the redox potential trends above, redox-sensitive metal (loid) concentrations mainly increase along the late shoulder season at the MIN and MOD sites, whereas at the EXT site, they are already elevated at the start of the campaign and remain high and stable throughout the season.

The Ge/Si ratio and δ^{30}Si isotope (Fig. 3h and i), by contrast, are indirect geochemical proxies that specifically track the dissolution of Fe-oxides, integrating the cumulative extent of Fe-oxide dissolution over the sampling interval rather than the instantaneous redox state (Delstanche et al., 2009; Pokrovsky et al., 2014). Consistent with the metal(loid) trends, Ge/Si increases progressively at the MIN and MOD sites, while at the EXT site it is already high and remains stable. However, δ^{30}Si values are significantly higher at the EXT than at the MIN site throughout the campaign highlighting freeze-thaw processes (Oelze et al., 2015).

Taken together, redox potential indicates when and how strongly reducing conditions develop, Fe, Mn, As and V concentrations track the immediate chemical consequence of reduction on metal(loid), while Ge/Si and δ^{30}Si indicate whether, and to what extent, these redox shifts translate into actual Fe-oxide dissolution. Rather than relying on any single line of evidence, combining these indicators strengthens confidence in the reconstructed redox dynamics: each parameter constrains a different part of the same process, and their consistency shows that the MIN and the MOD sites undergo an active seasonal redox transition, whereas the EXT site is already in a persistently reduced state.

4.2. Metal(loid) release along the late shoulder season from weakly to moderately reduced conditions

At the MIN and MOD sites, the progressive shift toward more reducing conditions promotes reductive dissolution of Fe-oxides and, at the MOD site, Mn-oxides present in the mineral horizon (Figs. 2b and 3c–e). As Mn(IV) reduction to soluble Mn(II) occurs under reduced conditions, this is consistent with Mn-oxide dissolution at the MOD site (Herndon et al., 2018; Li et al., 2021). Additionally, Mn-oxides are known to preferentially sorb and oxidize aromatic DOM compounds (Trainer et al., 2021). The reductive dissolution of Mn-oxides at the MOD site may therefore have simultaneously released aromatic DOC previously stabilized by Mn-oxides, potentially contributing to the observed increase in SUVA values (Fig. 3k). The absence of a Mn concentration increase at the MIN site therefore likely reflects a lower abundance of Mn-oxides available for reductive dissolution in the organic horizon compared to the mineral horizon at the MOD site, rather than a redox potential too high to trigger Mn reduction (Ji et al., 2021).

The Fe concentration increase at both sites (Fig. 3c) can be partly explained by the dissolution of Fe-oxides that are present in the bulk soil (up to 7000 mg kg^{-1} of Fe as Fe-oxides in the bulk soil; Monhonval et al., 2023) at the beginning of the late shoulder season. This is further supported by the V (MIN) and Ge/Si (MIN, MOD) trends noted above, since V and Ge preferentially adsorb onto Fe-oxide surfaces (Fig. 3e,i; Anders et al., 2003; Lim et al., 2022; Pang et al., 2025; Pokrovsky et al., 2014). The decrease in V concentrations at the MOD site suggests that processes other than oxide dissolution control V behavior. Under progressively reducing conditions, V may undergo redox transformations from the more mobile V(V) species to less soluble V(IV) or V(III), which are more readily adsorbed or incorporated into secondary mineral phases or organic matter (Pang et al., 2025).

The disparity in metal(loid) concentrations between soil water types likely arises from the fundamentally different nature of these two water pools (Fig. 3). Gravitational water represents a mixture of mobile waters draining through the soil profile, integrating microenvironments with contrasting redox conditions and receiving contributions from multiple water sources (Andresen et al., 2020; Fouché et al., 2021). During the late shoulder season, the progressive closure of hydrological pathways between capillary pore spaces and the gravitational water pool reduces the transfer of metal(loid)s mobilized at the pore scale into the broader gravitational water signal. This decoupling is reflected in the decreasing $\delta^{18}O$ values of well waters (Fig. 3l), which indicate a diminishing exchange with isotopically distinct capillary waters (Hirst et al., 2023). Well waters also integrate water over a broader depth interval (0–30 cm) compared to soil pore waters (at 30 cm depth), further contributing to these differences. In contrast, capillary waters retained within the immobile pore fraction of the soil matrix reflect strongly heterogeneous local physicochemical conditions, including localized redox microenvironments (Rezanezhad et al., 2016). In organic-rich soils, the dual-porosity structure (mobile and immobile pores) generates diffusion-limited solute exchanges that sustain strong physicochemical heterogeneity at the pore scale. Such geochemical contrasts between capillary and gravitational waters have been documented in other permafrost contexts, where soil pore waters showed significantly higher Fe, Mn, and As concentrations than gravitational waters, reflecting the more reducing and locally heterogeneous conditions captured by capillary waters (Skierszkan et al., 2024b). These observations highlight the importance of specifically targeting soil pore waters to capture localized redox changes that may be masked in well waters.

4.3. Stable and high metal(loid) concentration in soil pore waters during the late shoulder season under sustained moderately reduced conditions

At the EXT site, the persistently moderately reducing conditions along the late shoulder season (Fig. 2b) suggest that Fe-oxides are largely dissolved at the beginning of the late shoulder season in soil pore waters (Carneiro Barreto et al., 2024), as V, As, and Ge (over Si), adsorbed onto Fe-oxides, are released into the soil pore water upon their reductive dissolution (Skierszkan et al., 2024b).

As at the MIN site, the geochemical signal observed in soil pore waters at the EXT site does not translate into draining gravitational waters, likely due to the integrative and mixed nature of well waters discussed above. The contrasting $\delta^{30}Si$ values and Ge/Si values between soil pore waters and well waters at the EXT site provide an additional argument supporting this interpretation (Fig. 3h). The EXT site experiences more frequent freeze-thaw cycles during winter than the MIN and MOD sites, as supported by soil temperature data in March 2018 (Hirst et al., 2023; Kennedy et al., 2026). More specifically, during the month at 30 cm depth, soil temperature at the EXT site exceeded 0°C at least once within the day on 26 days (-0.1 ± 0.2°C), indicating repeated intraday zero-crossings, whereas this occurred on only 5 days at the MIN site (-0.4 ± 0.2°C) and did not occur at the MOD site (-0.9 ± 0.3°C). These freeze-thaw cycles induce Si isotopic fractionation through the preferential incorporation of light Si isotopes into amorphous silica particles precipitated upon freezing, leaving the residual soil pore water isotopically heavier (elevated $\delta^{30}Si$ values; Dietzel, 2005; Oelze et al., 2015). Simultaneously, because amorphous silica precipitation preferentially incorporates Si over Ge, the loss of Si from solution increases the Ge/Si ratio in the residual soil pore water (Fernandez et al., 2021; Opfergelt et al., 2024). As discussed above, Fe-oxide dissolution further elevates this ratio by releasing Ge (over Si) into soil pore waters (Anders et al., 2003). The absence of a Mn concentration increase in well waters despite the redox-sensitive conditions captured in soil pore waters is consistent with this same pore-to-well decoupling, whereby dilution and the reduced representation of localized reducing microenvironments limit the transfer of the pore water signal to the depth-integrated well water. This dilution effect, however, does not avoid a substantial absolute flux of metal(loid)s via gravitational water, as increased water flow paths associated with permafrost thaw can compensate for lower concentrations and still result in significant solute export to aquatic systems (Neilson et al., 2018; Toohey et al., 2016). Quantifying the relative contribution of soil pore water versus gravitational water fluxes at the catchment scale would require concurrent water flux measurements, and represents an important avenue for future work.

With continued permafrost thaw, the soil redox conditions across the site could shift towards those at the EXT site and subsequent predicted higher metal(loid) release with downstream impacts on river ecosystems (Grose et al., 2026; Krickov et al., 2026). This is consistent with the ongoing rusting of Arctic streams (when rivers turn orange; O'Donnell et al., 2024), a phenomenon already driving declines in macroinvertebrate diversity and fish abundance, with considerable implications for drinking water supplies and subsistence fisheries in rural Alaska.

4.4. Variability of DOC release along the late shoulder season

During the late shoulder season, multiple interacting processes drive changes in DOC in permafrost soils. Decreasing soil temperatures suppress microbial activity (Jansson and Taş, 2014), while decreasing oxygen availability promotes redox-sensitive mineral dissolution, releasing DOC through the destabilization of organo-metallic complexes and organic-mineral associations (Patzner et al., 2020). The contrasting redox conditions observed across study sites, in the organic horizon at the MIN site (higher soil water content; Fig. S2) and in the mineral horizon at the MOD and EXT sites (lower soil water content), suggest that the dominant mechanisms linking DOC and metal(loid) release differ between sites along the thaw gradient during the late shoulder season.

In the organic soil layer (MIN site; higher soil water content), the 50% increase in DOC concentration in soil pore waters (Fig. 3j) suggests enhanced DOC release under increasingly reducing conditions and associated Fe-oxide dissolution (Fig. 5). This pattern is consistent with

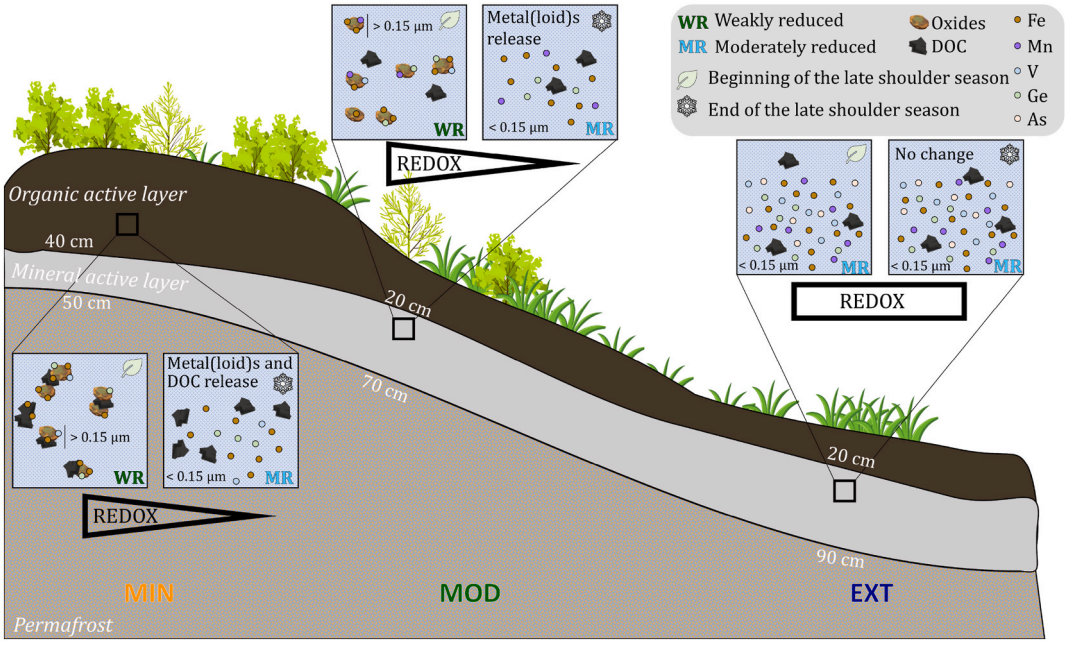


Fig. 5. Conceptual diagram summarizing the main processes occurring at the MIN, MOD, and EXT sites at 30 cm depth in the soil pore water (capillary water) during the late shoulder season. Processes occurring at the MIN site are in the organic layer, whereas processes at the MOD and EXT sites are in the mineral layer. At the MIN site, metal(loid) and DOC are released into the soil pore water along the late shoulder season, as redox potential shifts from weakly to moderately reduced. At the MOD site, metal(loid)s are released into the soil pore water along the late shoulder season, as redox potential shifts from weakly to moderately reduced. At the EXT site, metal(loid) and DOC concentrations remain high and stable in the soil pore water along the late shoulder season, as redox potential remains moderately reduced.

the destabilization of organo-metallic complexes (e.g., Fe–DOC complexes) and organo-mineral associations potentially linked to Fe-oxide dissolution (Herndon et al., 2017; Opfergelt, 2020; Opfergelt et al., 2026). This is supported by the coupling between DOC and Fe observed across permafrost regions of the Western Siberian Lowland, where colloidal transport of organo-ferric complexes has been identified as a dominant control on DOC and Fe mobilization (Krickov et al., 2026). The concurrent increase in Ge/Si values (Fig. 3i), positively correlated with DOC concentrations (Fig. S5a), further supports enhanced complexation between Ge and organic ligands (Slagter et al., 2026; Tarhan et al., 2025). Despite increasing DOC concentrations, SUVA values remain stable (Fig. 3k), suggesting that DOC release does not involve major changes in aromaticity (Gandois et al., 2019; Mann et al., 2015). In well waters, DOC concentration increase (Fig. 3j) indicates that the redox-driven processes may extend beyond the soil pore scale (Plaza et al., 2019). Given that well waters integrate mixed water sources, this DOC could be transported beyond the soil system and potentially contribute to downstream aquatic fluxes (Krickov et al., 2026; Vonk et al., 2019) . Furthermore, the coupling between DOC and Fe in the organic horizon may also leave a signature on the size of Fe-bearing nanoparticles: humic substances are known to inhibit the growth, transformation and ageing of Fe-oxyhydroxides, resulting in smaller nanoparticles (often < 50 nm; Moens et al., 2021). Consistently, the lower DOC concentrations at the Well MIN compared to the Well EXT site (Fig. 3j) at the beginning of the sampling period coincide with a higher Fe nanoparticle mass (i.e., estimated larger particle size) at this site (Figs. S7–8).

In contrast, in mineral soil layers (MOD and EXT sites; lower soil water content), DOC concentrations in soil pore water show no clear relationship with metal(loid)s concentrations (Fig. S5b–c), reflecting the lower abundance of organic functional groups available for complexation with metals or for organo-mineral associations compared to organic soils (Monhonval et al., 2023; Opfergelt, 2020). At the MOD site, this supports a decoupling between metal(loid) and DOC release, whereas at the EXT site, the comparatively stable metal(loid) and DOC concentrations reflect a decoupling of both from the change in redox potential, rather than a lack of interaction between metal(loid)s and DOC (Fig. 5). However, SUVA values increase significantly at the MOD site (and decrease significantly at the EXT site; Fig. 3k), indicating a shift toward more (or less) aromatic DOC forms, potentially affecting DOC mineralization (Gagné et al., 2020; Gandois et al., 2019). At the MOD site (mineral horizon), this change in DOC quality may be linked to redox-driven processes such as Mn-oxide dissolution, where Mn-oxides preferentially adsorbed aromatic DOC (Fig. 3d; Brüggenwirth et al., 2024; Trainer et al., 2021). At the EXT site (mineral horizon), sustained reducing conditions may have depleted Fe- and Mn-oxides prior to the late shoulder season, potentially limiting oxide-mediated retention and fractionation of aromatic DOC and contributing to the observed decrease in SUVA over the season.

Beyond their biogeochemical significance, these findings carry direct implications for the vulnerability of Arctic aquatic systems to permafrost thaw. In organic soils, the coupled release of metal(loid) and DOC reflects the dissolution of Fe-oxides that protect carbon from mobilization under oxic conditions, favoring potential C emission. In mineral soils, sustained or increasing metal(loid) concentrations under reducing conditions, even where DOC remains decoupled, point to an independent and potentially persistent source of metal(loid) release. As the late shoulder season lengthens under ongoing Arctic warming (Rantanen et al., 2022; Smith et al., 2022), the redox-driven mechanisms identified here are therefore expected to play an increasingly important role in shaping the quality and composition of water delivered to Arctic rivers and lakes (Krickov et al., 2026; Schuur et al., 2022; Strauss et al., 2025), with consequences for the ecosystems and communities that depend on them (Miner et al., 2021; O'Donnell et al., 2024).

5. Conclusion

Our results demonstrate that during the late shoulder season at Eight Mile Lake (Alaska, USA), metal(loid) and DOC release evolve differently depending on soil redox conditions in organic (higher soil water content) and mineral (lower soil water content) soil layers. Specifically, we show that:

- At less thawed sites, under weakly to moderately reducing conditions, metal(loid)s are released into soil pore waters at 30 cm depth. This release is coupled with DOC release in the organic soil layer (MIN site), whereas in the mineral soil layer (MOD site) DOC concentrations remain stable but shift toward more aromatic forms.
- At the more thawed site, under persistent moderately reducing conditions throughout the late shoulder season (EXT site), metal (loid) concentrations in soil pore waters at 30 cm depth remain stable and high. This suggests that the controlling processes likely involving metal(loid) release are already present at the beginning of the late shoulder season.
- In contrast to soil pore waters, freely draining waters (well waters) show limited variations in metal(loid) concentrations during the late shoulder season, likely due to the mixing of different water sources along the soil profile, which attenuates biogeochemical signals.

Overall, metal(loid) and DOC release in soil pore waters during the late shoulder season is strongly controlled by seasonal redox changes and by the distinction between organic (higher soil water content) and mineral (lower soil water content) soil layers. With ongoing Arctic warming, changes in soil hydrology and redox conditions along the late shoulder season may enhance metal(loid) and DOC transfer to aquatic systems. This release may have implications on water quality and carbon emissions.

CRediT authorship contribution statement

Maëlle Villani: Writing – review & editing, Writing – original draft, Visualization, Methodology, Investigation, Formal analysis, Conceptualization. **Catherine Hirst:** Writing – review & editing, Methodology, Formal analysis. **Eléonore du Bois d'Aische:** Writing – review & editing, Methodology, Formal analysis. **Cécile Osy:** Writing – review & editing, Methodology. **Maxime Thomas:** Writing – review & editing, Methodology. **Philippe Roux:** Writing – review & editing, Methodology, Formal analysis. **Marc F. Benedetti:** Writing – review & editing, Methodology, Formal analysis. **Justin Ledman:** Writing – review & editing, Methodology. **Edward Schuur:** Writing – review & editing, Methodology. **Sophie Opfergelt:** Writing – review & editing, Writing – original draft, Supervision, Project administration, Methodology, Investigation, Funding acquisition, Formal analysis, Conceptualization.

Declaration of generative AI and AI-assisted technologies in the manuscript preparation process

During the preparation of this work the author(s) used ChatGPT and Claude in order to improve language clarity and rephrase sentences. After using this tool/service, the author(s) reviewed and edited the content as needed and take(s) full responsibility for the content of the published article.

Declaration of competing interest

The authors declare that they have no known competing financial interests or personal relationships that could have appeared to influence the work reported in this paper.

Acknowledgments

We acknowledge the support of the Center for Ecosystem Science and Society (ECOSS) for facilitating access to the study site. We thank the analytical platform MOCA at UCLouvain, and the valuable input from the LandSense team K. Van Oost, V. Vanacker, F. Jonard and S. Lambot (Action de Recherche Concertée (ARC), no. 21/26–119, funded by the Fédération Wallonie-Bruxelles (FWB)). We thank M. Tharaud for his help during Fe NPs measurements. We acknowledge funding from the European Research Council (ERC) under the European Union's Horizon 2020 research and innovation programme (ERC Starting Grant, WeThaw, n°714617) to S.O, from the Fonds National de la Recherche Scientifique to S.O., M.V. and E. d.B.A. (FNRS: FC69480, FC49507, and FC54613), from BELSPO (RT/23/LIFTHAW), from CircleU (Seed funding CEDRIC), and from the Royal Academy of Belgium (Fonds Agathon de Potter) to M.T. We thank the editor, Jon Petter Gustafsson, and two anonymous reviewers for their valuable comments.

Appendix A. Supplementary data

Supplementary data to this article can be found online at https://doi.org/10.1016/j.apgeochem.2026.107179.

Data availability

The data related to this article is available online at: https://doi.org/10.14428/DVN/TEWGBB.

References

Abraham, K., Opfergelt, S., Fripiat, F., Cavagna, A.-J., De Jong, J.T.M., Foley, S.F., André, L., Cardinal, D., 2008. δ30Si and δ29Si determinations on USGS BHVO-1 and BHVO-2 reference materials with a new configuration on a Nu plasma Multi-Collector ICP-MS. Geostand. Geoanal. Res. 32 (2), 193–202. https://doi.org/10.1111/j.1751-908X.2008.00879.x.

Anders, A.M., Sletten, R.S., Derry, L.A., Hallet, B., 2003. Germanium/silicon ratios in the Copper River Basin, Alaska : weathering and partitioning in periglacial versus glacial environments. J. Geophys. Res. Earth Surf. 108 (F1). https://doi.org/10.1029/2003JF000026.

Andresen, C.G., Lawrence, D.M., Wilson, C.J., McGuire, A.D., Koven, C., Schaefer, K., Jafarov, E., Peng, S., Chen, X., Gouttevin, I., Burke, E., Chadburn, S., Ji, D., Chen, G., Hayes, D., Zhang, W., 2020. Soil moisture and hydrology projections of the permafrost region – a model intercomparison. Cryosphere 14 (2), 445–459. https://doi.org/10.5194/tc-14-445-2020.

Arndt, K.A., Hashemi, J., Natali, S.M., Schiferl, L.D., Virkkala, A.-M., 2023. Recent advances and challenges in monitoring and modeling non-growing season carbon dioxide fluxes from the Arctic Boreal Zone. Curr. Clim. Change Rep. 9 (2), 27–40. https://doi.org/10.1007/s40641-023-00190-4.

Barczok, M., Smith, C., Kinsman-Costello, L., Patzner, M., Bryce, C., Kappler, A., Singer, D., Herndon, E., 2024. Iron transformation mediates phosphate retention across a permafrost thaw gradient. Commun. Earth Environ. 5 (1), 1–11. https://doi.org/10.1038/s43247-024-01810-z.

Barker, A.J., Douglas, T.A., Jacobson, A.D., McClelland, J.W., Ilgen, A.G., Khosh, M.S., Lehn, G.O., Trainor, T.P., 2014. Late season mobilization of trace metals in two small Alaskan arctic watersheds as a proxy for landscape scale permafrost active layer dynamics. Chem. Geol. 381, 180–193. https://doi.org/10.1016/j.chemgeo.2014.05.012.

Barker, A.J., Sullivan, T.D., Baxter, W.B., Barbato, R.A., Gallaher, S., Patton, G.E., Smith, J.P., Douglas, T.A., 2023. Iron oxidation–reduction processes in warming permafrost soils and surface waters expose a seasonally rusting Arctic watershed. ACS Earth Space Chem. 7 (8), 1479–1495. https://doi.org/10.1021/acsearthspacechem.2c00367.

Bergman, O., Walter Anthony, K., Eliani-Russak, E., Sivan, O., 2025. Nitrogen Redox controls on greenhouse gas production in Yedoma taliks. Glob. Change Biol. 31 (7), e70356. https://doi.org/10.1111/gcb.70356.

Brüggenwirth, L., Behrens, R., Schnee, L.S., Sauheitl, L., Mikutta, R., Mikutta, C., 2024. Interactions of manganese oxides with natural dissolved organic matter : implications for soil organic carbon cycling. Geochem. Cosmochim. Acta 366, 182–200. https://doi.org/10.1016/j.gca.2023.12.016.

Cardinal, D., Alleman, L.Y., Jong, J. de, Ziegler, K., André, L., 2003. Isotopic composition of silicon measured by multicollector plasma source mass spectrometry in dry plasma mode. J. Anal. At. Spectrom. 18 (3), 213–218. https://doi.org/10.1039/B210109B.

Carneiro Barreto, M.S., Wani, R.P., Goranov, A.I., Sowers, T.D., Fischel, M., Douglas, T. A., Hatcher, P.G., Sparks, D.L., 2024. Carbon fate, iron dissolution, and molecular characterization of dissolved organic matter in thawed Yedoma permafrost under varying redox conditions. Environ. Sci. Technol. https://doi.org/10.1021/acs.est.3c08219 acs.est.3c08219.

Catrouillet, C., Davranche, M., Dia, A., Bouhnik-Le Coz, M., Demangeat, E., Gruau, G., 2016. Does As(III) interact with Fe(II), Fe(III) and organic matter through ternary complexes? J. Colloid Interface Sci. 470, 153–161. https://doi.org/10.1016/j.jcis.2016.02.047.

Chupakov, A.V., Pokrovsky, O.S., Moreva, O.Y., Kotova, E.I., Vorobyeva, T.Y., Shirokova, L.S., 2023. Export of organic carbon, nutrients and metals by the mid-sized Pechora River to the Arctic Ocean. Chem. Geol. 632, 121524. https://doi.org/10.1016/j.chemgeo.2023.121524.

Cornelis, G., Hassellöv, M., 2014. A signal deconvolution method to discriminate smaller nanoparticles in single particle ICP-MS. J. Anal. At. Spectrom. 29 (1), 134–144. https://doi.org/10.1039/C3JA50160D.

Delstanche, S., Opfergelt, S., Cardinal, D., Elsass, F., André, L., Delvaux, B., 2009. Silicon isotopic fractionation during adsorption of aqueous monosilicic acid onto iron oxide. Geochem. Cosmochim. Acta 73 (4), 923–934. https://doi.org/10.1016/j.gca.2008.11.014.

Dial, R.J., Hanna, C.T., Sullivan, P.F., Cooper, D.J., Tino, C.J., Gregory, D.D., Diamond, C., Rieser, M., Nicolsky, D.J., Hill, K., Iwahana, G., Koch, J.C., Carey, M.P., Miller, L., Lyons, T.W., 2026. Permafrost thaw controls iron flux from wetlands and sulfide-bearing rocks to Arctic rivers and streams. Commun. Earth Environ. 7 (1), 465. https://doi.org/10.1038/s43247-026-03450-x.

Dietzel, M., 2005. Impact of cyclic freezing on precipitation of silica in Me–SiO2–H2O systems and geochemical implications for cryosoils and -sediments. Chem. Geol. 216 (1), 79–88. https://doi.org/10.1016/j.chemgeo.2004.11.003.

Drake, T.W., Raymond, P.A., Spencer, R.G.M., 2018. Terrestrial carbon inputs to inland waters : a current synthesis of estimates and uncertainty. Limnol. Oceanogr. Lett. 3 (3), 132–142. https://doi.org/10.1002/lol2.10055.

Duan, X., Li, Z., Wang, S., Mason-Jones, K., Wei, L., Chen, X., Wu, J., Ge, T., Zhu, Z., 2025. Stability of iron-carbon complexes determines carbon sequestration efficiency in iron-rich soils. Soil Biol. Biochem. 203, 109718. https://doi.org/10.1016/j.soilbio.2025.109718.

Fernandez, N.M., Perez-Fodich, A., Derry, L.A., Druhan, J.L., 2021. A first look at Ge/Si partitioning during amorphous silica precipitation : implications for Ge/Si as a tracer of fluid-silicate interactions. Geochem. Cosmochim. Acta 297, 158–178. https://doi.org/10.1016/j.gca.2021.01.007.

Fernandez, P.M., Bloem, E., Binley, A., Philippe, R.S.B.A., French, H.K., 2019. Monitoring redox sensitive conditions at the groundwater interface using electrical resistivity and self-potential. J. Contam. Hydrol. 226, 103517. https://doi.org/10.1016/j.jconhyd.2019.103517.

Fouché, J., Bouchez, C., Keller, C., Allard, M., Ambrosi, J.-P., 2021. Seasonal cryogenic processes control supra-permafrost pore water chemistry in two contrasting Cryosols. Geoderma 401, 115302. https://doi.org/10.1016/j.geoderma.2021.115302.

Gagné, K., Ewers, C., J, S., Murphy, C., Daanen, R., Anthony, K.W., GuerardJ, J., 2020. Composition and photo-reactivity of organic matter from permafrost soils and surface waters in interior Alaska. Environ. Sci. Process. Impacts 22 (7), 1525–1539. https://doi.org/10.1039/D0EM00097C.

Gandois, L., Hoyt, A.M., Hatté, C., Jeanneau, L., Teisserenc, R., Liotaud, M., Tananaev, N., 2019. Contribution of Peatland Permafrost to dissolved organic matter along a thaw gradient in North Siberia. Environ. Sci. Technol. 53 (24), 14165–14174. https://doi.org/10.1021/acs.est.9b03735.

Gartler, S., Scheer, J., Meyer, A., Abass, K., Bartsch, A., Doloisio, N., Falardeau, J., Hugelius, G., Irrgang, A., Haukur Ingimundarson, J., Jungsberg, L., Lantuit, H., Nymand Larsen, J., Lodi, R., Martin, V.S., Mercer, L., Nielsen, D., Overduin, P., Povoroznyuk, O., et al., 2025. A transdisciplinary, comparative analysis reveals key risks from Arctic permafrost thaw. Commun. Earth Environ. 6 (1), 21. https://doi.org/10.1038/s43247-024-01883-w.

Georg, R.B., Reynolds, B.C., Frank, M., Halliday, A.N., 2006. New sample preparation techniques for the determination of Si isotopic compositions using MC-ICPMS. Chem. Geol. 235 (1), 95–104. https://doi.org/10.1016/j.chemgeo.2006.06.006.

Gorny, J., Billon, G., Lesven, L., Dumoulin, D., Madé, B., Noiriel, C., 2015. Arsenic behavior in river sediments under redox gradient : a review. Sci. Total Environ. 505, 423–434. https://doi.org/10.1016/j.scitotenv.2014.10.011.

Grose, A.L., Zarnetske, J.P., Grewal, A., Shogren, A.J., Rec, A.F., O'Donnell, J.A., Abbott, B.W., Bowden, W.B., 2026. Tracing seasonal ground thaw with stream chemistry in Alaskan Arctic Permafrost catchments. Hydrol. Process. 40 (4), e70512. https://doi.org/10.1002/hyp.70512.

Herndon, E., AlBashaireh, A., Singer, D., Roy Chowdhury, T., Gu, B., Graham, D., 2017. Influence of iron redox cycling on organo-mineral associations in Arctic tundra soil. Geochem. Cosmochim. Acta 207, 210–231. https://doi.org/10.1016/j.gca.2017.02.034.

Herndon, E., Kinsman-Costello, L., Godsey, S., 2020. Biogeochemical cycling of redox-sensitive elements in Permafrost-Affected ecosystems. In: Biogeochemical Cycles. American Geophysical Union (AGU), pp. 245–265. https://doi.org/10.1002/9781119413332.ch12.

Herndon, E.M., Havig, J.R., Singer, D.M., McCormick, M.L., Kump, L.R., 2018. Manganese and iron geochemistry in sediments underlying the redox-stratified Fayetteville Green Lake. Geochem. Cosmochim. Acta 231, 50–63. https://doi.org/10.1016/j.gca.2018.04.013.

Hirst, C., Monhonval, A., Mauclet, E., Thomas, M., Villani, M., Ledman, J., Schuur, E.A.G., Opfergelt, S., 2023. Evidence for late winter biogeochemical connectivity in permafrost soils. Commun. Earth Environ. 4 (1), 1. https://doi.org/10.1038/s43247-023-00740-6.

Hughes, Harold J., Delvigne, Camille, Korntheuer, Michael, de Jong, Jeroen, André, Luc, Cardinal, Damien, 2011. Controlling the mass bias introduced by anionic and organic matrices in silicon isotopic measurements by MC-ICP-MS. Journal of Analytical Atomic Spectrometry 26 (9), 1892. https://doi.org/10.1039/c1ja10110b. https://pubs.rsc.org/ja/article/26/9/1892-1896/350419.

Jansson, J.K., Taş, N., 2014. The microbial ecology of permafrost. Nat. Rev. Microbiol. 12 (6), 414–425. https://doi.org/10.1038/nrmicro3262.

Jentzsch, K., Männistö, E., Marushchak, M.E., Korrensalo, A., van Delden, L., Tuittila, E.-S., Knoblauch, C., Treat, C.C., 2024. Shoulder season controls on methane emissions from a boreal peatland. Biogeosciences 21 (16), 3761–3788. https://doi.org/10.5194/bg-21-3761-2024.

Ji, X., Abakumov, E., Polyakov, V., Xie, X., 2021. Mobilization of geochemical elements to surface water in the active layer of Permafrost in the Russian arctic. Water Resour. Res. 57 (1), e2020WR028269. https://doi.org/10.1029/2020WR028269.

Kappler, A., Bryce, C., Mansor, M., Lueder, U., Byrne, J.M., Swanner, E.D., 2021. An evolving view on biogeochemical cycling of iron. Nat. Rev. Microbiol. 19 (6), 360–374. https://doi.org/10.1038/s41579-020-00502-7.

Kelley, A.K., Pegoraro, E., Mauritz, M., Hutchings, J.A., Natali, S., Hicks-Pries, C.E., Schuur, E.A.G., 2021. Eight Mile Lake Research Watershed, Thaw Gradient : Seasonal Thaw Depth 2004-2020. Bonanza Creek LTER. https://doi.org/10.6073/PASTA/BEB6635175CBCE79C9F83DDF657075EE.

Kennedy, E., Celis, G., See, C., Schaedel, C., Mauritz, M., Taylor, M., Ledman, J., Natali, S., Schuur, E.A.G., 2026. Eight Mile Lake Research Watershed : Hourly Meteorological Data, 2004-2025. Bonanza Creek LTER - University of Alaska Fairbanks. https://doi.org/10.6073/pasta/c1b76570a7f3d4feaef428e98970b2be. BNZ:453.

Kleber, M., Bourg, I.C., Coward, E.K., Hansel, C.M., Myneni, S.C.B., Nunan, N., 2021. Dynamic interactions at the mineral–organic matter interface. Nat. Rev. Earth Environ. 2 (6), 402–421. https://doi.org/10.1038/s43017-021-00162-y.

Krickov, I.V., Loiko, S.V., Lim, A.G., Kuzmina, D.M., Istigechev, G.I., Shirokova, L.S., Pupyshev, Y.S., Pokrovsky, O.S., 2026. Hydrological continuums across climate and permafrost gradients : spatial patterns of organic carbon, greenhouse gases, and major and trace elements. Water Res. 294, 125507. https://doi.org/10.1016/j.watres.2026.125507.

Kritzberg, E.S., Villanueva, A.B., Jung, M., Reader, H.E., 2014. Importance of boreal Rivers in providing iron to marine waters. PLoS One 9 (9), e107500. https://doi.org/10.1371/journal.pone.0107500.

Li, H., Santos, F., Butler, K., Herndon, E., 2021. A critical review on the multiple roles of manganese in stabilizing and destabilizing soil organic matter. Environ. Sci. Technol. 55 (18), 12136–12152. https://doi.org/10.1021/acs.est.1c00299.

Liebmann, P., Vogel, C., Kholodov, A., Bárta, J., Waqas, M., Varsadiya, M., Wang, H., Urich, T., Mansfeldt, T., Wessel-Bothe, S., Shibistova, O., Guggenberger, G., 2025. Perennial redox potential dynamics in Alaskan degraded and non-degraded permafrost soils. Commun. Earth Environ. 7 (1), 120. https://doi.org/10.1038/s43247-025-03143-x.

Lim, A.G., Loiko, S.V., Kuzmina, D.M., Krickov, I.V., Shirokova, L.S., Kulizhsky, S.P., Pokrovsky, O.S., 2022. Organic carbon, and major and trace elements reside in labile low-molecular form in the ground ice of permafrost peatlands : a case study of colloids in peat ice of Western Siberia. Environ. Sci. Process. Impacts 24 (9), 1443–1459. https://doi.org/10.1039/D1EM00547B.

Mann, P.J., Eglinton, T.I., McIntyre, C.P., Zimov, N., Davydova, A., Vonk, J.E., Holmes, R.M., Spencer, R.G.M., 2015. Utilization of ancient permafrost carbon in headwaters of Arctic fluvial networks. Nat. Commun. 6 (1), 7856. https://doi.org/10.1038/ncomms8856.

Mauclet, E., Agnan, Y., Hirst, C., Monhonval, A., Pereira, B., Vandeuren, A., Villani, M., Ledman, J., Taylor, M., Jasinski, B.L., Schuur, E.A.G., Opfergelt, S., 2022. Changing sub-Arctic tundra vegetation upon permafrost degradation : impact on foliar mineral element cycling. Biogeosciences 19 (9), 2333–2351. https://doi.org/10.5194/bg-19-2333-2022.

Mauritz, M., Bracho, R., Celis, G., Hutchings, J., Natali, S.M., Pegoraro, E., Salmon, V.G., Schädel, C., Webb, E.E., Schuur, E.A.G., 2017. Nonlinear CO2 flux response to 7 years of experimentally induced permafrost thaw. Glob. Change Biol. 23 (9), 3646–3666. https://doi.org/10.1111/gcb.13661.

Miner, K.R., D'Andrilli, J., Mackelprang, R., Edwards, A., Malaska, M.J., Waldrop, M.P., Miller, C.E., 2021. Emergent biogeochemical risks from Arctic permafrost degradation. Nat. Clim. Change 11 (10), 809–819. https://doi.org/10.1038/s41558-021-01162-y.

Moens, C., Montalvo, D., Smolders, E., 2021. The concentration and size distribution of iron-rich colloids in pore waters are related to soil organic matter content and pore water calcium concentration. Eur. J. Soil Sci. 72 (5), 2199–2214. https://doi.org/10.1111/ejss.13104.

Monhonval, A., Mauclet, E., Hirst, C., Bemelmans, N., Eekman, E., Schuur, E.A.G., Opfergelt, S., 2023. Mineral organic carbon interactions in dry versus wet tundra soils. Geoderma 436, 116552. https://doi.org/10.1016/j.geoderma.2023.116552.

Moreira-Álvarez, B., Cid-Barrio, L., Calderón-Celis, F., Costa-Fernández, J.M., Encinar, J. R., 2023. Relative and transport efficiency-independent approach for the determination of nanoparticle size using single-particle ICP-MS. Anal. Chem. 95 (27), 10430–10437. https://doi.org/10.1021/acs.analchem.3c01823.

Mueller, C.W., Rethemeyer, J., Kao-Kniffin, J., Löppmann, S., Hinkel, K.M., Bockheim, J. G., 2015. Large amounts of labile organic carbon in permafrost soils of northern Alaska. Glob. Change Biol. 21 (7), 2804–2817. https://doi.org/10.1111/gcb.12876.

Mueller, M.H., Alaoui, A., Kuells, C., Leistert, H., Meusburger, K., Stumpp, C., Weiler, M., Alewell, C., 2014. Tracking water pathways in steep hillslopes by δ18O depth profiles of soil water. J. Hydrol. 519, 340–352. https://doi.org/10.1016/j.jhydrol.2014.07.031.

Natali, S., Schuur, E.A.G., Rubin, R.L., 2012. Increased plant productivity in Alaskan tundra as a result of experimental warming of soil and permafrost. J. Ecol. 100 (2), 488–498. https://doi.org/10.1111/j.1365-2745.2011.01925.x.

Natali, S., Schuur, E.A.G., Trucco, C., Hicks Pries, C.E., Crummer, K.G., Baron Lopez, A. F., 2011. Effects of experimental warming of air, soil and permafrost on carbon balance in Alaskan tundra. Glob. Change Biol. 17 (3), 1394–1407. https://doi.org/10.1111/j.1365-2486.2010.02303.x.

Neilson, B.T., Cardenas, M.B., O'Connor, M.T., Rasmussen, M.T., King, T.V., Kling, G.W., 2018. Groundwater flow and exchange across the land surface explain carbon export patterns in continuous Permafrost watersheds. Geophys. Res. Lett. 45 (15), 7596–7605. https://doi.org/10.1029/2018GL078140.

O'Donnell, J.A., Carey, M.P., Koch, J.C., Baughman, C., Hill, K., Zimmerman, C.E., Sullivan, P.F., Dial, R., Lyons, T., Cooper, D.J., Poulin, B.A., 2024. Metal mobilization from thawing permafrost to aquatic ecosystems is driving rusting of

Arctic streams. Commun. Earth Environ. 5 (1), 268. https://doi.org/10.1038/s43247-024-01446-z.
O'Donnell, J.A., Romanovsky, V., Harden, J.W., McGuire, A.D., 2009. The Effect of Moisture Content on the Thermal.Soil Sci. https://doi.org/10.1097/SS.0b013e3181c4a7f8. Ovid.
Obu, J., 2021. How much of the Earth's surface is underlain by Permafrost? J. Geophys. Res. Earth Surf. 126 (5), e2021JF006123. https://doi.org/10.1029/2021JF006123.
Oelze, M., von Blanckenburg, F., Bouchez, J., Hoellen, D., Dietzel, M., 2015. The effect of Al on Si isotope fractionation investigated by silica precipitation experiments. Chem. Geol. 397, 94–105. https://doi.org/10.1016/j.chemgeo.2015.01.002.
Opfergelt, S., 2020. The next generation of climate model should account for the evolution of mineral-organic interactions with permafrost thaw. Environ. Res. Lett. 15 (9), 091003. https://doi.org/10.1088/1748-9326/ab9a6d.
Opfergelt, S., Gaspard, F., Hirst, C., Monin, L., Juhls, B., Morgenstern, A., Angelopoulos, M., Overduin, P.P., 2024. Frazil ice changes winter biogeochemical processes in the Lena River. Commun. Earth Environ. 5 (1), 1–8. https://doi.org/10.1038/s43247-024-01884-9.
Opfergelt, S., Herndon, E., Bryce, C., Hirst, C., 2026. Iron as a driver of organic carbon fate in permafrost regions. Nat. Geosci. https://doi.org/10.1038/s41561-026-02015-z.
Osterkamp, T.E., Jorgenson, M.T., Schuur, E.a.G., Shur, Y.L., Kanevskiy, M.Z., Vogel, J. G., Tumskoy, V.E., 2009. Physical and ecological changes associated with warming permafrost and thermokarst in Interior Alaska. Permafr. Periglac. Process. 20 (3), 235–256. https://doi.org/10.1002/ppp.656.
PAC, 1972. Manual of symbols and terminology for physicochemical quantities and units, Appendix II: definitions. In: Terminology and Symbols in Colloid and Surface Chemistry, vol. 31.
Pang, X., Zhang, B., Zhang, Q., Jiang, J., 2025. Freeze–Thaw cycling accelerates microbial reduction and immobilization of Vanadium(V) in groundwater. Environ. Sci. Technol. 59 (47), 25278–25287. https://doi.org/10.1021/acs.est.5c11332.
Patzner, M.S., Kainz, N., Lundin, E., Barczok, M., Smith, C., Herndon, E., Kinsman-Costello, L., Fischer, S., Straub, D., Kleindienst, S., Kappler, A., Bryce, C., 2022. Seasonal fluctuations in iron cycling in thawing permafrost peatlands. Environ. Sci. Technol. 56 (7), 4620–4631. https://doi.org/10.1021/acs.est.1c06937.
Patzner, M.S., Mueller, C.W., Malusova, M., Baur, M., Nikeleit, V., Scholten, T., Hoeschen, C., Byrne, J.M., Borch, T., Kappler, A., Bryce, C., 2020. Iron mineral dissolution releases iron and associated organic carbon during permafrost thaw. Nat. Commun. 11 (1), 6329. https://doi.org/10.1038/s41467-020-20102-6.
Perryman, C.R., Wirsing, J., Bennett, K.A., Brennick, O., Perry, A.L., Williamson, N., Ernakovich, J.G., 2020. Heavy metals in the Arctic : distribution and enrichment of five metals in Alaskan soils. PLoS One 15 (6), e0233297. https://doi.org/10.1371/journal.pone.0233297.
Plaza, C., Pegoraro, E., Bracho, R., Celis, G., Crummer, K.G., Hutchings, J.A., Hicks Pries, C.E., Mauritz, M., Natali, S.M., Salmon, V.G., Schädel, C., Webb, E.E., Schuur, E.A.G., 2019. Direct observation of permafrost degradation and rapid soil carbon loss in tundra. Nat. Geosci. 12 (8), 8. https://doi.org/10.1038/s41561-019-0387-6.
Pokrovsky, O.S., Galy, A., Schott, J., Pokrovski, G.S., Mantoura, S., 2014. Germanium isotope fractionation during Ge adsorption on goethite and its coprecipitation with Fe oxy(hydr)oxides. Geochem. Cosmochim. Acta 131, 138–149. https://doi.org/10.1016/j.gca.2014.01.023.
Pokrovsky, O.S., Manasypov, R.M., Loiko, S.V., Shirokova, L.S., 2016. Organic and organo-mineral colloids in discontinuous permafrost zone. Geochem. Cosmochim. Acta 188, 1–20. https://doi.org/10.1016/j.gca.2016.05.035.
Poulin, B.A., Ryan, J.N., Aiken, G.R., 2014. Effects of iron on optical properties of dissolved organic matter. Environ. Sci. Technol. 48 (17), 10098–10106. https://doi.org/10.1021/es502670r.
Rantanen, M., Karpechko, A.Y., Lipponen, A., Nordling, K., Hyvärinen, O., Ruosteenoja, K., Vihma, T., Laaksonen, A., 2022. The Arctic has warmed nearly four times faster than the globe since 1979. Commun. Earth Environ. 3 (1), 1. https://doi.org/10.1038/s43247-022-00498-3.
Reddy, K.R., DeLaune, R.D., Inglett, P.W., 2022. Biogeochemistryof Wetlands : Science and Applications. CRC press.
Reynolds, B.C., Aggarwal, J., André, L., Baxter, D., Beucher, C., Brzezinski, M.A., Engström, E., Georg, R.B., Land, M., Leng, M.J., Opfergelt, S., Rodushkin, I., Sloane, H.J., Boorn, S., Vroon, P.Z., Cardinal, D., 2007. An inter-laboratory comparison of Si isotope reference materials. J. Anal. At. Spectrom. 22 (5), 561–568. https://doi.org/10.1039/B616755A.
Rezanezhad, F., Price, J.S., Quinton, W.L., Lennartz, B., Milojevic, T., Van Cappellen, P., 2016. Structure of peat soils and implications for water storage, flow and solute transport : a review update for geochemists. Chem. Geol. 429, 75–84. https://doi.org/10.1016/j.chemgeo.2016.03.010.
Schuur, E.A.G., Abbott, B.W., Commane, R., Ernakovich, J., Euskirchen, E., Hugelius, G., Grosse, G., Jones, M., Koven, C., Leshyk, V., Lawrence, D., Loranty, M.M., Mauritz, M., Olefeldt, D., Natali, S., Rodenhizer, H., Salmon, V., Schädel, C., Strauss, J., et al., 2022. Permafrost and climate change : carbon cycle feedbacks from the warming Arctic. Annu. Rev. Environ. Resour. 47 (1), 343–371. https://doi.org/10.1146/annurev-environ-012220-011847.
Schuur, E.A.G., Crummer, K.G., Vogel, J.G., Mack, M.C., 2007. Plant species composition and productivity following Permafrost thaw and Thermokarst in Alaskan tundra. Ecosystems 10 (2), 280–292. https://doi.org/10.1007/s10021-007-9024-0.
Shaheen, S.M., Alessi, D.S., Tack, F.M.G., Ok, Y.S., Kim, K.-H., Gustafsson, J.P., Sparks, D. L., Rinklebe, J., 2019. Redox chemistry of vanadium in soils and sediments : interactions with colloidal materials, mobilization, speciation, and relevant environmental implications- A review. Adv. Colloid Interface Sci. 265, 1–13. https://doi.org/10.1016/j.cis.2019.01.002.
Shogren, A.J., Zarnetske, J.P., Abbott, B.W., Iannucci, F., Bowden, W.B., 2020. We cannot shrug off the shoulder seasons : addressing knowledge and data gaps in an Arctic headwater. Environ. Res. Lett. 15 (10), 104027. https://doi.org/10.1088/1748-9326/ab9d3c.
Skierszkan, E.K., Carey, S.K., Jackson, S.I., Fellwock, M., Fraser, C., Lindsay, M.B.J., 2024a. Seasonal controls on stream metal(loid) signatures in mountainous discontinuous permafrost. Sci. Total Environ. 908, 167999. https://doi.org/10.1016/j.scitotenv.2023.167999.
Skierszkan, E.K., Schoepfer, V.A., Fellwock, M.D., Dockrey, J.W., Hayatifar, A., Bondici, V.F., McBeth, J.M., Lindsay, M.B.J., 2024b. Arsenic mobilization from thawing permafrost. ACS Earth Space Chem. 8 (4), 745–759. https://doi.org/10.1021/acsearthspacechem.3c00355.
Skierszkan, E.K., Szeitz, A.J., Lindsay, M.B.J., Carey, S.K., 2026. Abrupt stream acidification and metal mobilization from permafrost degradation. Science 392 (6800), 863–867. https://doi.org/10.1126/science.aea2898.
Slagter, S., Asael, D., Planavsky, N.J., Perez-Fodich, A., Tarhan, L.G., 2026. Experimental Ge/Si partitioning during organic-mediated silica precipitation. Chem. Geol. 699, 123156. https://doi.org/10.1016/j.chemgeo.2025.123156.
Smith, S.L., O'Neill, H.B., Isaksen, K., Noetzli, J., Romanovsky, V.E., 2022. The changing thermal state of permafrost. Nat. Rev. Earth Environ. 3 (1), 10–23. https://doi.org/10.1038/s43017-021-00240-1.
Soil, Survey Staff, 1999. Soil Taxonomy : a Basic System of Soil Classification for Making and Interpreting Soil Surveys, vol. 436. U.S. Gov. Print. Off.. https://www.nrcs.usda.gov/Internet/FSE_DOCUMENTS/nrcs142p2_051232.pdf
Strauss, J., Fuchs, M., Hugelius, G., Miesner, F., Nitze, I., Opfergelt, S., Schuur, E., Treat, C., Turetsky, M., Yang, Y., Grosse, G., 2025. Organic matter storage and vulnerability in the permafrost domain. In: Elias, S. (Ed.), Encyclopedia of Quaternary Science, third ed. Elsevier, pp. 399–410. https://doi.org/10.1016/B978-0-323-99931-1.00164-1.
Street, L.E., Dean, J.F., Billett, M.F., Baxter, R., Dinsmore, K.J., Lessels, J.S., Subke, J.-A., Tetzlaff, D., Wookey, P.A., 2016. Redox dynamics in the active layer of an Arctic headwater catchment; examining the potential for transfer of dissolved methane from soils to stream water. J. Geophys. Res. Biogeosci. 121 (11), 2776–2792. https://doi.org/10.1002/2016JG003387.
Sutor, F.W., Roy, E.D., Schroth, A.W., Michaud, A.B., Emerson, D., Herndon, E.M., Kinsman-Costello, L., Hurley, S.E., Bowden, W.B., 2025. Geochemical Phosphorus sequestration in Tundra Soils impedes delivery of bioavailable Phosphorus to the Kuparuk River, Alaska, USA : implications for the broader Arctic Region. J. Geophys. Res. Biogeosci. 130 (10), e2025JG008803. https://doi.org/10.1029/2025JG008803.
Tan, H., Wen, X., Rao, W., Bradd, J., Huang, J., 2016. Temporal variation of stable isotopes in a precipitation–groundwater system : implications for determining the mechanism of groundwater recharge in high mountain–hills of the Loess Plateau, China. Hydrol. Process. 30 (10), 1491–1505. https://doi.org/10.1002/hyp.10729.
Tarhan, L.G., Hood, A.v.S., Droser, M.L., 2025. Elevated marine dissolved Silica levels explain a wide range of Ediacaran–Cambrian Ediacara-Style fossil deposits. Geobiology 23 (2), e70017. https://doi.org/10.1111/gbi.70017.
Tharaud, M., Gondikas, A.P., Benedetti, M.F., Kammer, F., Hofmann, T., Cornelis, G., 2017. TiO2 nanomaterial detection in calcium rich matrices by spICPMS. A matter of resolution and treatment. J. Anal. At. Spectrom. 32 (7), 1400–1411. https://doi.org/10.1039/C7JA00060J.
Tharaud, M., Louvat, P., Benedetti, M.F., 2021. Detection of nanoparticles by single-particle ICP-MS with complete transport efficiency through direct nebulization at few-microlitres-per-minute uptake rates. Anal. Bioanal. Chem. 413 (3), 923–933. https://doi.org/10.1007/s00216-020-03048-y.
Toohey, R.C., Herman-Mercer, N.M., Schuster, P.F., Mutter, E.A., Koch, J.C., 2016. Multidecadal increases in the Yukon River Basin of chemical fluxes as indicators of changing flowpaths, groundwater, and permafrost. Geophys. Res. Lett. 43 (23). https://doi.org/10.1002/2016GL070817, 12,120-12,130.
Trainer, E.L., Ginder-Vogel, M., Remucal, C.K., 2021. Selective reactivity and oxidation of dissolved organic matter by manganese oxides. Environ. Sci. Technol. 55 (17), 12084–12094. https://doi.org/10.1021/acs.est.1c03972.
Villani, M., Hirst, C., du Bois d'Aische, E., Osy, C., Thomas, M., Roux, P., Lundin, E., Ledman, J., Schuur, E.A.G., Opfergelt, S., 2026. The late shoulder season modifies the mobility of iron and dissolved organic carbon in rivers from distinct permafrost regions. Chem. Geol. 724, 123707. https://doi.org/10.1016/j.chemgeo.2026.123707.
Villani, M., Hirst, C., du Bois d'Aische, E., Thomas, M., Opfergelt, S., Lundin, E., Giesler, R., Mörth, C.-M., 2025. Lengthening of biogeochemical processes during winter in degraded permafrost soils. Geochem. Perspect. Lett. 34 (34), 36–42.
Villani, M., Mauclet, E., Agnan, Y., Druel, A., Jasinski, B., Taylor, M., Schuur, E.A.G., Opfergelt, S., 2022. Mineral element recycling in topsoil following permafrost degradation and a vegetation shift in sub-Arctic tundra. Geoderma 421, 115915. https://doi.org/10.1016/j.geoderma.2022.115915.
Vogel, J., Schuur, E.A.G., Trucco, C., Lee, H., 2009. Response of CO2 exchange in a tussock tundra ecosystem to permafrost thaw and thermokarst development. J. Geophys. Res. Biogeosci. 114 (G4). https://doi.org/10.1029/2008JG000901.
Vonk, J.E., Tank, S.E., Walvoord, M.A., 2019. Integrating hydrology and biogeochemistry across frozen landscapes. Nature Communications 10 (1), 5377. https://doi.org/10.1038/s41467-019-13361-5. https://www.nature.com/articles/s41467-019-13361-5. (Accessed 26 November 2019).
Wallis, I., Prommer, H., Berg, M., Siade, A.J., Sun, J., Kipfer, R., 2020. The river–groundwater interface as a hotspot for arsenic release. Nat. Geosci. 13 (4), 288–295. https://doi.org/10.1038/s41561-020-0557-6.
Walvoord, M.A., Striegl, R.G., 2007. Increased groundwater to stream discharge from permafrost thawing in the Yukon River basin : potential impacts on lateral export of

carbon and nitrogen. Geophys. Res. Lett. 34 (12). https://doi.org/10.1029/2007GL030216.
Wauthy, M., Rautio, M., Christoffersen, K.S., Forsström, L., Laurion, I., Mariash, H.L., Peura, S., Vincent, W.F., 2018. Increasing dominance of terrigenous organic matter in circumpolar freshwaters due to permafrost thaw. Limnol. Oceanogr. Lett. 3 (3), 186–198. https://doi.org/10.1002/lol2.10063.
Weyhenmeyer, G.A., Prairie, Y.T., Tranvik, L.J., 2014. Browning of boreal freshwaters coupled to carbon-iron interactions along the aquatic continuum. PLoS One 9 (2), e88104. https://doi.org/10.1371/journal.pone.0088104.
Wigginton, N.S., Haus, K.L., Jr, M.F.H., 2007. Aquatic environmental nanoparticles. J. Environ. Monit. 9 (12), 1306–1316. https://doi.org/10.1039/B712709J.
Yang, L., Zou, Y., Jiang, M., Yu, Z., 2025. Permafrost enhances association of minerals with organic carbon in anoxic environments of peatlands. Environ. Res. 282, 122100. https://doi.org/10.1016/j.envres.2025.122100.
Yeghicheyan, D., Carignan, J., Valladon, M., Le Coz, M.B., Cornec, F.L., Castrec-Rouelle, M., Robert, M., Aquilina, L., Aubry, E., Churlaud, C., Dia, A., Deberdt, S., Dupré, B., Freydier, R., Gruau, G., Hénin, O., de Kersabiec, A.-M., Macé, J., Marin, L., et al., 2001. A compilation of silicon and thirty one trace elements measured in the natural River water reference material SLRS-4 (NRC-CNRC). Geostand. Newsl. 25 (2–3), 465–474. https://doi.org/10.1111/j.1751-908X.2001.tb00617.x.